Master thesis : Modelisation of aero-optic effects in supersonic conditions

Auteur : Lafontaine, Pierre
Promoteur(s) : Terrapon, Vincent
Faculté : Faculté des Sciences appliquées
Diplôme : Master en ingénieur civil en aérospatiale, à finalité spécialisée en "aerospace engineering"
Année académique : 2017-2018
URI/URL : http://hdl.handle.net/2268.2/4545

University of Liège - Faculty of Applied Sciences

Academic year 2017-2018

Modelisation of aero-optic effects in supersonic conditions

Graduation Studies conducted for obtaining the Master's degree in Aerospace Engineering by Pierre Lafontaine.

Abstract

Optical distortions are observed everywhere, in nature and in man-crafted technologies. These distortions affect the performances of the optical systems, and as such present an interest to be studied.

In the context of an airborne optical device, the optical perturbations are mostly due to the near-field perturbation of the flow. Considering a supersonic flow, the perturbed region is limited by a shock wave. This region, in which the optical aberrations are generated is therefore clearly defined.

A missile optical guidance system is chosen as a model for the simulations.

Acknowledging the importance of aerodynamic heating through shocks and heat exchanges in the boundary layer, a fluid-structure interaction simulation is performed. The density field of the flow can be directly related to the index of refraction; the increase of temperature of the optical window induce a modification of the index of refraction, and thermo-elastic deformations occurs due to the increase of temperature.

The surface of the shock wave is fitted by a polynomial surface: it is expected to provide a good characterization of the optical effect of the shock. The optical performances of the system under aero-optic disturbances are computed by sequential ray tracing, considering two wavelength of light: infrared ($\lambda = 4$ [μm]) and ultraviolet ($\lambda = 0.25$ [μm]).

The results are consistent with the expected optical effects of the aberrations, and show that the heating of the optical window dominates the deterioration of the optical performances. For an hemispherical window in a flow of Mach 4 and an angle of view of 20°, the boresight shift is equal to 0.57 [mrad]. The UV signal is largely blurred by the optical aberrations, while the infrared shows focus errors close to its limit of diffraction in the system considered.

The successful computation of aberrations in the same order of magnitude as reference simulations supports the importance of the characterization of the shock surface.

Acknowledgements

First of all I would like to thank Open-Engineering for giving me the opportunity to conduct this work as a part of my internship. Obviously, thanks to the team ! I greatly appreciated your kindness and your useful tips.

Special thanks to J.M. Vaassen and P. Saint-Georges, for your help, for the tremendous amount of explanations and advices you provided, and for your patience.

Finally I would like to thank all the people that supported me throughout my cursus.

Contents

Chapter 1

Introduction

Optical distortions can be observed everywhere, in nature and in man crafted technologies. They directly affect the performances of high-end technologies, such as stars observation, laser systems or micro-opto-electro-mechanical systems (MOEMS). Airborne optical systems were particularly developed in the last decades, and new applications continue to emerge, with for example a renewed interest in laser communications. However a constant limitation is the presence of a perturbed flow near the optical systems; it induces aero-optical perturbations which affect the performances of the device.

These aero-optical distortions can be directly related to variations of density in the flow field. Indeed the Gladstone-Dale relation (Equ. 5.1.14 in Sec. 5.1) relates the refractive index of a fluid to its density. An additional source of optical perturbances appears in high speed flows, where an important aerodynamic heating occurs through shocks. The increase of temperature of the fluid is followed by a partial heating of the body, i.e. of the optical system. As a consequence, variations of the index of refraction an thermo-mechanical deformations may occur, having a direct effect on the optical performances. In more extreme conditions, the temperatures of the gases may increase to an extent that the flow emit radiations in bandwidth that could interfere with the signal being transmitted.

The modelling of all the aero-optical effects is technically challenging as it involves several strongly coupled physical phenomena. An accurate description of the density field may be required in order to represent the smallest length scales (density field due to small scale turbulence) which may interact with the signal.

The previous works conducted on aero-optic effects, including numerical simulations and experimental studies, highlighted that the nature and intensity of optical disturbances are strongly linked with the nature of the flow. In subsonic flow the aerodynamic heating is negligible, and most of the disturbances are induced by vortices and turbulence structures in the flow near the optical window. Several studies, notably Mathews ([**aero_optics_LES**]) or Ladd ([JB]), shown good accordance of the modelled optical performances with experiments by performing a Large eddy simulation of the flow.

On the other hand, the optical disturbances in supersonic flows are dominated by the density gradient through the shock and by the aerodynamic heating of the air and of the optical window. The optical perturbations produced by developed turbulent boundary layers are also non negligible

as shown by Gordeyev ([S G15]). LES simulations are proved to provide consistent modelling of the related optical disturbances (Zilberter [ZE]). As studied by Tropf ([Tro+87]), the re-radiation of the hot gases towards the optical sensor is non negligible for hypersonic flows. However the related decrease of signal-to-noise ratio is expected to decrease with the Mach number of the flow.

The objective of this work is to simulate the optical performances of a supersonic airborne system and to characterize the aero-optic effects observed. Acknowledging the importance of heat fluxes between the flow and the optical device, a fluid-structure interaction simulation shall be performed. The FSI scheme is based on communications between the thermo-mechanical solver of `OOFELIE::Multiphysics` and the fluid solver of `FINE™/Open`. A processing of the obtained results is performed by a dedicated code, implemented as a part of this work. The shock wave is detected and its surface is fitted by an analytical expression. The perturbed region of the flow behind the shock is identified and extracted as a set of discrete values. The optical performances of the system are modelled by ray tracing in `Zemax OpticStudio`. In the optical model, non homogeneous temperature and density fields of the fluid and solid domains are represented by gradient of index (GRIN) materials. The thermo-mechanical deformations computed as a part of the FSI solution are applied to the corresponding parts of the model.

The optical performances obtained at the end of the workflow shall be discussed in terms of consistency with the theoretical expectations. The nature and order of magnitude of the optical perturbations computed are compared with the results of other works in order to assess qualitatively the quality of the optical performance modelling.

Chapter 2

Methodology

In the context of airborne devices, most of the optical aberrations originate from the perturbation of the near field flow by the body. The present work aims to take advantage of the presence of a shock wave to define the region of perturbed flow.

In high energy flows, complex phenomena such as molecular dissociation and chemical reactions may take place; these phenomena are highly complex to model and could be alone the subject of a dedicated work. The flow conditions in the present work are therefore restricted to strictly supersonic speeds in order to reduce the number of physical fields involved. This allows to take the convenient assumption that the fluid behaves as a calorically perfect gas and is in chemical equilibrium.

A focus is considered on the modelling of the steady aero-optic effects on the optical performances. The flow is therefore assumed steady and uniform away from the body. The different turbulence scales are modelled by time-averaging; the fluid solution is obtained by resolution of RANS equations, which constitutes a great diminution of computational cost compared to LES simulations. A steady solution also disregard the unsteady, highly complex problem of shock-turbulence interactions and shock perturbation modelling. The study is conducted in 3D.

Among the existing shock configurations, the bow shock appears to be a good case for aero-optic disturbances modelling: an air layer with a non uniform density and temperature fields lie behind the shock (see Sec.3.1). An appealing physical configuration promoting such shock is the case of an optical sensor located behind an hemispherical optical window, facing the supersonic flow. Another great asset of this configuration is the absence of incoming boundary layer as it would be the case for an optical turret fixed on a fuselage. Under realistic operational conditions for such shape (low angles of attack, smooth geometry of the body), a boundary layer separation or other complex turbulent phenomena can be easily avoided in the region of interest. A typical optical airborne device corresponding to such geometry is a missile optical guidance system; the dimensions and material of the solid model are therefore inspired from a very famous supersonic infrared guided missile, the FIM-92 "Stinger". Its operational conditions in terms of speed and wavelengths used by the sensor are used to define the fluid and optic model.

The modelling of the optical disturbances and of the underlying multiphysics problem relies on the transfer and processing of the respective solutions of 3 computer programs according to the scheme depicted in Fig. 2.0.1:

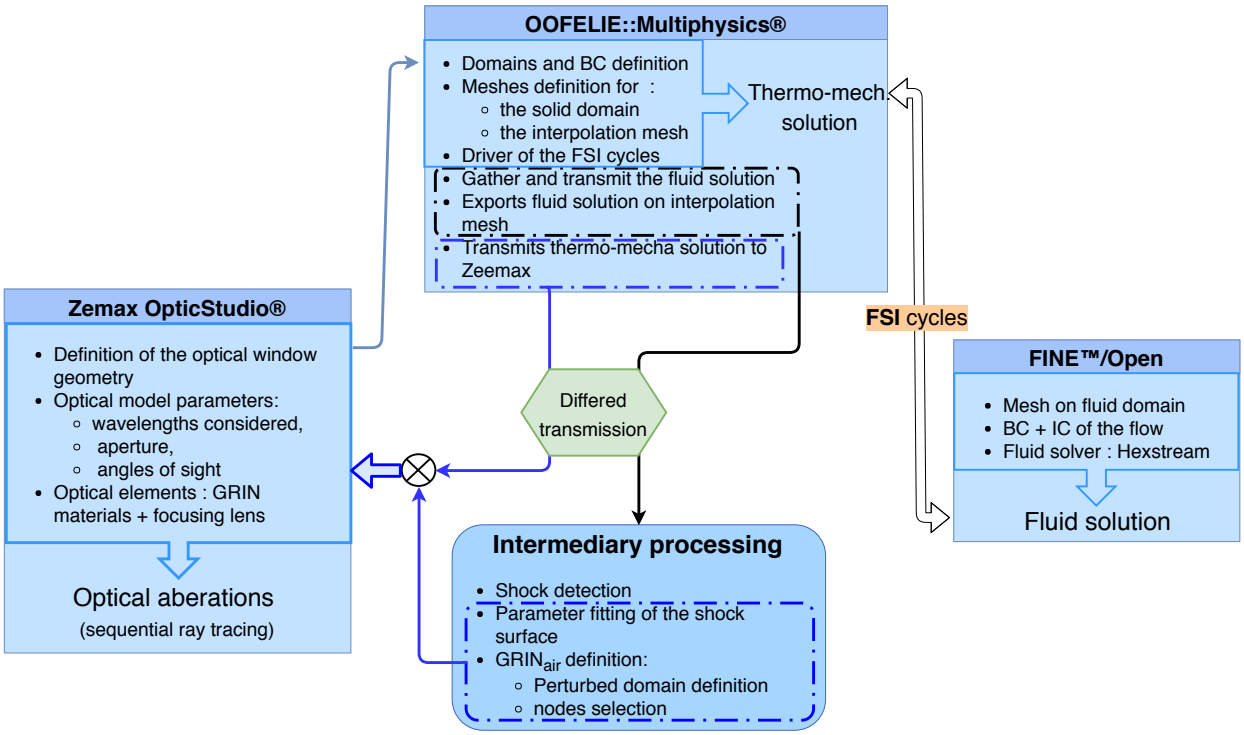

Figure 2.0.1: Scheme of the software interactions leading to the optical disturbances computation, including differed transmission to the developed post-processing code.

The fluid-structure interaction (FSI) resolution scheme consists in exchanges between the respective solvers of `OOFELIE::Multiphysics` and `FINE™/Open`. The solvers communicate by Message Passing Interface (MPI); the transmission of solutions between the structural and fluid mesh is performed by an interpolation method based on the Catmull-Clark subdivision method.

The solutions are then processed before being sent to a third program, `Zemax`, which models the optical performances of the system by ray tracing.

The deflection of light rays is directly related to the presence of variations of the index of refraction (see Equ. 5.1.11: such gradients of refractive index (GRIN) are created inside the different media considered due to non homogeneity of the properties. The interface between two media of different optical properties is indeed also charaterized by gradients of refractive index.

Modelling of the shock and air layer The flow density, pressure and temperature increase abruptly after the shock (refers to Sec. 3.1), proportionally to the shock strength. Since the density of a fluid can be directly related to its refractive index (see Gladstone-Dale equation, Equ. 5.1.14), this index also increase abruptly through the shock. There are therefore

- strong gradients of index of refraction in the shock,
- a layer of air with non homogeneous refractive index between the shock wave and the optical window.

The processing of the fluid results aims to determine a subset of nodes defining the GRIN layer, and to detect and characterize the shock surface. These methods were developed as a part of this work, and aims to be integrated in a more automated workflow in the future.

Two approaches are considered for modelling the GRIN_{air}:

1. the shockwave presents strong gradients and is assumed to have an important effect on the optical aberrations. It is therefore considered primordial to provide a good characterization of its surface. To do so, the shock is detected using an appropriate criterion. A least squares error parameter fitting of the detected shock coordinates is then performed for an appropriate function. The obtained surface bounds the perturbed flow; the GRIN_{air} medium is defined as the air layer between the shock and the optical surface.
2. The second approach does represent the shock surface explicitly. During the computation of the ray propagation, the value of the index of refraction is successively evaluated along the ray trajectory; therefore the variations of index of refraction are directly considered by the optical modeller.

The two methods are to be compared in terms of the results produced, attended that both of them introduce errors in the modelling.

Modelling of the optical window Heat fluxes between the flow and the structure increase the temperature of the optical window. This produces two effects: a non homogeneous variation of the temperature leading to a GRIN_{window}, and thermo-mechanical deformations.

The total optical aberrations related to the index of refraction can be defined as the combined contributions of $GRIN_{air}$ and $GRIN_{window}$.

Other sources of optical disturbances exists and could be taken into account: according to [Tro+87] the infrared radiations emitted by the hot gases (particularly H_20 and CO_2) and by the heated optical window produce disturbances on the optical sensor. Particularly, they increase the signal-to-noise ratio perceived by the sensor. This radiation also participates to raise the temperature of the sensor, and further increases the background radiation. However these two radiating effects were also shown to be only moderately significant in hypersonic flows: a fraction of the standard atmospheric background radiation. For slower flows these effects are further reduced since the increase of temperature through the shock is Mach-dependant (see Equ. 3.1.13 in Sec. 3.1.1). These radiating effects are therefore not considered.

Chapter 3

Fluid-structure interaction: a multiphysic problem

In subsonic aerodynamics, the phenomenon of flow heating by compression and dissipation is so weak that it is generally neglected. However when supersonic speeds are reached in the flow, shock waves occurs, associated notably with an increase of the temperature of the fluid. Such aerodynamic heating can become very significant, and the thermal interaction between the flow and the structure must be considered.

A mechanical coupling between the fluid and the structure is always present is real structures; however the present work considers a steady problem (no aeroelasticity considerations), and the solid body is considered sufficiently rigid for not being subject to high deformation under the flow pressure. On the other hand, the deformations are assumed to be sufficiently small for not having an influence on the flow over the structure. MPI communications between the fluid and the thermo-mechanical solvers, in respectively `FINE™/Open` and `OOFELIE`, define the FSI computation scheme.

In the present chapter, the theoretical considerations behind the fluid and thermo-mechanical solutions are exposed. It allows to determine an acceptable level of modelling and thus the definition of rather simple solid and fluid domains. The boundary conditions determining the solutions to the governing equations are issued from the operational conditions of the missile taken as an inspiration. Several flow configurations are considered, corresponding to different angles of attack of the body; a case with a higher Mach number is also treated. The numerical schemes and the coupling strategy between the two solvers are briefly exposed, before a presentation of the different results.

3.1 Theoretical background

3.1.1 Generalities about the flow considered

The flow considered is steady, compressible and viscous. The gas considered is air in low altitude standard conditions, and is assumed to behave as an inert perfect gas.

As such, the speed of sound in the fluid a can be expressed as $a = \sqrt{\gamma RT}$. The Mach number of the flow is defined as $M = \dfrac{\boldsymbol{V}}{a}$, with $\boldsymbol{V}$ the local airspeed. A flow is supersonic if its local airspeed is greater than its local speed of sound, i.e. if $M = 1$.

The flow parameters are issued from the operational conditions of the model: the freestream Mach number is $M_{\text{inf}} = 2.5$.

Governing equations

The general equations describing the dynamics of a steady, viscous flow are, as developed in [And01]:

Continuity:

$$\frac{\partial(\rho u)}{\partial x} + \frac{\partial(\rho v)}{\partial y} + \frac{\partial(\rho w)}{\partial z} = 0 \tag{3.1.1}$$

Momentum:

$$\begin{aligned}
\frac{\partial(\rho u^2)}{\partial x} + \frac{\partial(\rho uv)}{\partial y} + \frac{\partial(\rho uw)}{\partial z} &= -\frac{\partial p}{\partial x} + \frac{\partial \tau_{xx}}{\partial x} + \frac{\partial \tau_{yx}}{\partial y} + \frac{\partial \tau_{zx}}{\partial z} \\
\frac{\partial(\rho uv)}{\partial x} + \frac{\partial(\rho v^2)}{\partial y} + \frac{\partial(\rho vw)}{\partial z} &= -\frac{\partial p}{\partial x} + \frac{\partial \tau_{xy}}{\partial x} + \frac{\partial \tau_{yy}}{\partial y} + \frac{\partial \tau_{zy}}{\partial z} \\
\frac{\partial(\rho uw)}{\partial x} + \frac{\partial(\rho vw)}{\partial y} + \frac{\partial(\rho w^2)}{\partial z} &= -\frac{\partial p}{\partial x} + \frac{\partial \tau_{xz}}{\partial x} + \frac{\partial \tau_{yz}}{\partial y} + \frac{\partial \tau_{zz}}{\partial z}
\end{aligned} \tag{3.1.2}$$

Energy:

$$\begin{aligned}
\frac{\partial \rho uE}{\partial x} + \frac{\partial \rho vE}{\partial y} + \frac{\partial \rho wE}{\partial z} = \quad & \rho\dot{q} + \frac{\partial}{\partial x}\Big(k\frac{\partial T}{\partial x}\Big) + \frac{\partial}{\partial y}\Big(k\frac{\partial T}{\partial y}\Big) + \frac{\partial}{\partial z}\Big(k\frac{\partial T}{\partial z}\Big) - \nabla \cdot p\mathbf{V} \\
& + \frac{\partial(u\tau_{xx})}{\partial x} + \frac{\partial(u\tau_{yx})}{\partial y} + \frac{\partial(u\tau_{zx})}{\partial z} + \frac{\partial(v\tau_{xy})}{\partial x} + \frac{\partial(v\tau_{yy})}{\partial y} \\
& + \frac{\partial(v\tau_{zy})}{\partial z} + \frac{\partial(w\tau_{xz})}{\partial x} + \frac{\partial(w\tau_{yz})}{\partial y} + \frac{\partial(w\tau_{zz})}{\partial z}
\end{aligned} \tag{3.1.3}$$

where

$$\begin{aligned}
\tau_{xy} &= \mu\Big(\frac{\partial v}{\partial x} + \frac{\partial u}{\partial y}\Big) \\
\tau_{yz} &= \mu\Big(\frac{\partial w}{\partial y} + \frac{\partial v}{\partial z}\Big) \\
\tau_{zx} &= \mu\Big(\frac{\partial u}{\partial z} + \frac{\partial w}{\partial x}\Big) \\
\tau_{xx} &= \lambda(\nabla \cdot \mathbf{V}) + 2\mu\frac{\partial u}{\partial x} \\
\tau_{yy} &= \lambda(\nabla \cdot \mathbf{V}) + 2\mu\frac{\partial v}{\partial y} \\
\tau_{zz} &= \lambda(\nabla \cdot \mathbf{V}) + 2\mu\frac{\partial w}{\partial z}
\end{aligned} \tag{3.1.4}$$

In these equations,

- u, v, w are the components of $\boldsymbol{V}(\boldsymbol{r}, t)$,
- p, ρ, μ are the pressure ($[\mathrm{N} \cdot \mathrm{m}^{-2}]$), density ($[\mathrm{kg} \cdot \mathrm{m}^{-3}]$) and dynamic viscosity ($[\mathrm{N} \cdot \mathrm{s} \cdot \mathrm{m}^{-2}]$) of the fluid,
- E is the total energy ([J]) of the flow,
- q is the external heat flux ($[\mathrm{W} \cdot \mathrm{m}^{-2}]$).

However the direct simulation of complex turbulent flows is very difficult in engineering applications; a partitioning of the flow between mean and fluctuating parts is required. To this end, the Reynolds Averaged Navier Stokes (RANS) equations are derived from the Navier-Stokes (NS) equations by averaging over a time interval T. The flow quantities can therefore be decomposed between an average and a perturbation component as follows: for any quantity A,

$$A = \overline{A} + A^{'},$$

Note that the energy, velocity components and temperature are density-weighted time averaged: $A = \tilde{A} + A^{"}$, with

$$\tilde{A} = \frac{\overline{\rho A}}{\overline{\rho}}$$

The Reynolds decomposition of the stress and heat flux terms in Equ. 3.1.2 and Equ. 3.1.3 leads to the introduction of the Reynolds stress tensor and turbulent heat diffusion terms, which are the perturbation components of the original terms. These quantities being unknown, a model of the underlying physics is required in order to close the set of equations.

The closure model used for turbulence is based on Boussinesq's assumption: introducing the eddy-viscosity μ_t, a linear relation is considered between the Reynolds-stress tensor and the mean flow strain:

$$-\left(\overline{\rho \mathbf{v}^{"} \otimes \mathbf{v}^{"}}\right) = \mu_t \Big[2\mathbf{S} - \frac{2}{3}\big(\nabla \cdot \tilde{\mathbf{v}}\big)\mathbf{I}\Big] - \frac{2}{3}\overline{\rho} k \mathbf{I} \tag{3.1.5}$$

where

- $\overline{\rho \mathbf{v}^{"} \otimes \mathbf{v}^{"}}$ is the Reynolds stress tensor, appearing after averaging the momentum and energy equations,
- $\mathbf{S}$ is the mean strain tensor,
- k is the turbulent kinetic energy,
- μ_t is the turbulent eddy viscosity.

A turbulence model defining μ_t must therefore be provided: the Spalart-Allmaras turbulence model[1] is used in the present work.

The turbulent heat flux vector must also be defined. Introducing the turbulent thermal conductivity κ_t, it can be connected to the previously defined turbulent eddy-viscosity μ_t through a turbulent Prandtl number Pr_t, writing:

$$\overline{\rho h^{"} \mathbf{v}^{"}} = -\kappa_t \nabla T \quad \text{where} \quad \kappa_t = \frac{\mu_t c_p}{Pr_t}. \tag{3.1.6}$$

Shock waves

Supersonic flows have a strong characteristic: they are dominated by shock waves. The physical mechanism behind such waves can be explained as follows: the molecules impacting the body surface undergo a change in momentum; this change is transmitted to neighbouring molecules at the local speed of sound. The upstream flow being supersonic, the disturbances can not propagate upstream: they pile up and coalesce, forming a standing wave. This shock wave is an extremely thin region ($10^{-}7$ [m] in air at standard atmospheric conditions according to Anderson [And01]) of high gradients across which the flow properties change drastically. These abrupt, almost discontinuous variations are characterized by the Rankine-Hugoniot jump relations. As derived from the Navier-Stokes equations in [And01], they write, for an oblique shock:

$$\rho_2 u_2 = \rho_1 u_1 \tag{3.1.7}$$

$$\rho_2 u_2^2 + p_2 = \rho_1 u_1^2 + p1 \tag{3.1.8}$$

$$h_2 + \frac{1}{2}u_2^2 = h_1 + \frac{1}{2}u_1^2, \tag{3.1.9}$$

where

- ρ_i is the fluid density,
- u_{ni} is the airspeed normal to the shock surface,
- h_i is the enthalpy

of the medium i, as depicted in Fig. 3.1.1.

[1] A more complete description is provided in Appendix A.1

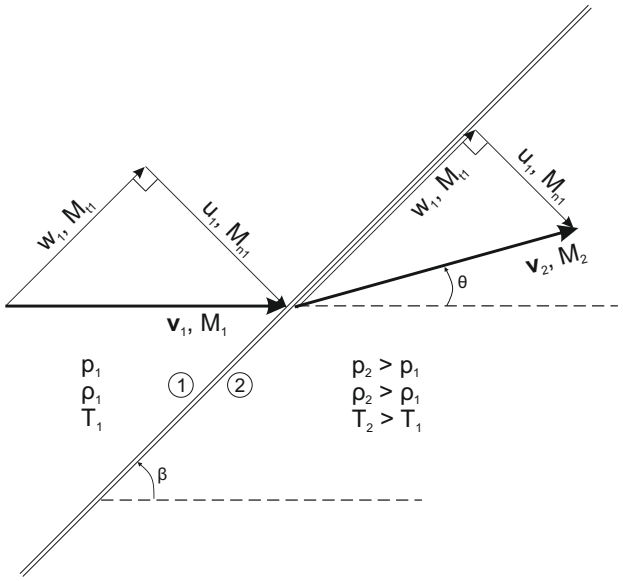

Figure 3.1.1: Representation of an oblique shock and qualitative description of the flow properties variation.

It can be noticed that changes across an oblique shock wave are governed only by the velocity component normal to the shock. On the other hand, the tangential component of the flow velocity is constant across an oblique shock.

These relations (Equ. 3.1.7 to 3.1.9) can be expressed in terms of the normal component of the upstream Mach number $M_{n,1} = M_1 \sin\beta$, β being the angle between the shock and the free stream velocity direction:

$$M_{n,2}^2 = \frac{1 + [(\gamma-1)/2]M_{n,1}}{\gamma M_{n,1}^2 - (\gamma-1)/2} \tag{3.1.10}$$

$$\frac{\rho_2}{\rho_1} = \frac{(\gamma+1)M_{n,1}^2}{2 + (\gamma-1)M_{n,1}^2} \tag{3.1.11}$$

$$\frac{p_2}{p_1} = 1 + \frac{2\gamma}{\gamma+1}(M_{n,1}^2 - 1) \tag{3.1.12}$$

$$\frac{T_2}{T_1} = \frac{p_2}{p_1}\frac{\rho_1}{\rho_2} \tag{3.1.13}$$

The shape and location of the shock depend on the Mach number and the physical geometry: in 2D, the relationship between the deflection angle of the flow θ , the angle of the resulting oblique shock β and the Mach number of the flow M_1 is described by Equ. 3.1.14:

$$\tan\theta = 2\cot\beta\Big(\frac{M_1^2\sin\beta^2 - 1}{M_1^2(\gamma + \cos 2\beta) + 2}\Big) \tag{3.1.14}$$

Note that this relations stands for the deflection of 2D flows, or 3D flows around a body of constant profile along the 3^{rd} dimension (wedge). For other bodies, a 3D relieving effect decreases the shock angle: the flow over the body has an extra dimension in which to be deflected. However Equ. 3.1.14 still provides a good insight of the flow deflection-shock angle relation in terms of possible solutions.

It defines for a given M_1 a maximum deflection angle θ_{max} for which a solution exists, i.e. for which the resulting shock is oblique and attached to the body. If the physical geometry is such that $\theta > \theta_{max}$, there is no solution for a straight oblique shock wave. This defines the body as "blunt" with respect to the flow, such as it requires a deflection of the flow that exceeds the maximum admissible deflection angle.

In this case the shock will be curved and detached from the body, forming a so-called bow shock, as represented in Fig. 3.1.2. One see that the shock is detached from the body, with a stand off distance δ and a region of subsonic flow.

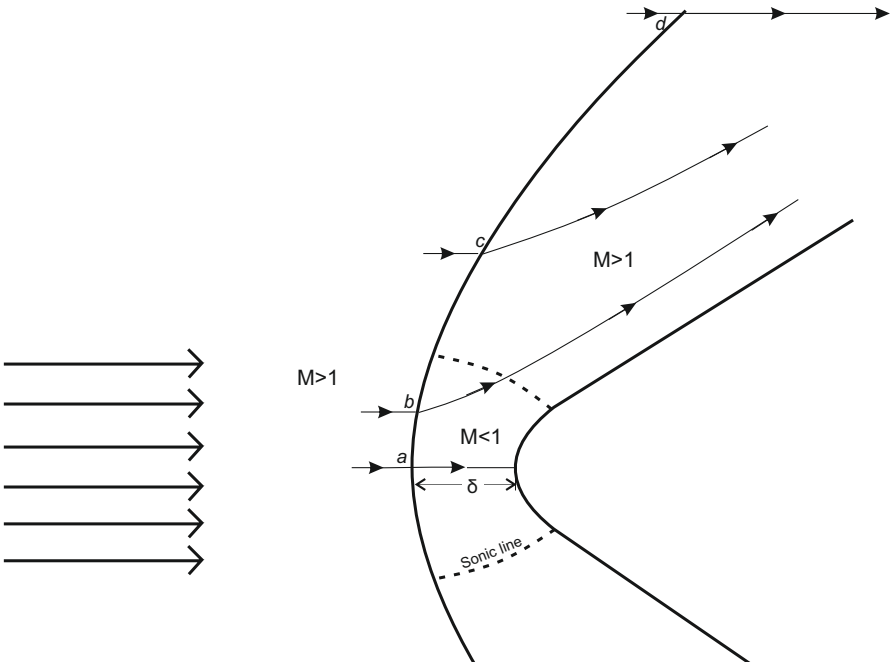

Figure 3.1.2: Representation of the flow over a supersonic blunt body.

The shock is indeed normal to the upstream flow at a, resulting in very strong gradients and a reduction of the Mach number below 1. It becomes gradually more oblique and thus weaker away from the body. It eventually evolves into a Mach wave a large distances from the body, forming a Mach angle μ with the flow, with $\sin\mu = 1/M_\infty$. Since the strength of the shock vary along the location on the shock, the jump in flow quantities vary as well: there is a gradient in flow properties after the shock wave. Indeed according to Equ. 3.1.10 the jump in temperature, pressure and density is higher at a than at b, and higher at b than at c.

Due to the mixed subsonic and supersonic regions in the flow field, the shock shape and the flow behind such shock are complex and cannot be solved analytically. However experiments have allowed to establish empirical relations predicting with some success the shape of the shock wave over blunt bodies.

As used in [Tro+87], Equ. 3.1.15 defines a shape that may be used in practice to define the region of interest in the computational domain:

$$z = R + \Delta - R_c \text{cotan}^2\theta \Big[\Big(1 + \frac{y^2 \tan^2 \theta}{R_c^2} \Big)^{1/2} - 1 \Big] \tag{3.1.15}$$

with

- R is the radius of curvature of the leading edge,
- Δ_0 is the stand off distance, computed by $\Delta = 0.143R \exp\Big(\frac{3.24}{M_\infty^2}\Big)$,
- $R_c = 1.143R \exp\Big(\frac{0.54}{(M-1)^{1.2}}\Big)$,
- θ is the free stream Mach angle in the case of a uniform body after the leading edge.

3.1.2 Governing thermo-elastic equations

The body considered is surrounded by a flow in which an increase of temperature occurs. Inevitably, a certain amount of thermal energy is exchanged between the flow and the structure. The resulting temperature field is the solution of the heat diffusion equation, which writes from [Fra12], under steady-state conditions and considering no internal energy generation, as Equ. 3.1.16:

$$\frac{\partial}{\partial x}\Big(k\frac{\partial T}{\partial x}\Big) + \frac{\partial}{\partial y}\Big(k\frac{\partial T}{\partial y}\Big) + \frac{\partial}{\partial z}\Big(k\frac{\partial T}{\partial z}\Big) = \rho c_p \frac{\partial T}{\partial t}. \tag{3.1.16}$$

Such solution depends on the physical conditions present at the boundaries of the medium; these thermal boundaries conditions are defined in Sec. 3.3.1.

An important consequence of the increase of temperature of the structure is the generation of thermo-mechanical stresses. These stresses σ_{ij} and the subsequent deformations of the structure ϵ_{ij} are related by the Duhamel-Neumann law (Equ. 3.1.17), as developed in [Ces01]:

$$\sigma_{ij} = \frac{E}{(1+\nu)(1-2\nu)}[(1-2\nu)\epsilon_{ij} + \nu\epsilon_{ll}\delta_{ij}] - \beta\delta_{ij}\Delta T, \tag{3.1.17}$$

where

- E is the Young's modulus [$\text{N} \cdot \text{m}^{-2}$],
- ν is the Poisson's coefficient [-],
- β is the thermal expansion coefficient [K^{-1}].

In order to obtain this form, the materials are assumed to be isotropic and to undergo small displacements. All these parameters are considered at the reference temperature $T_0 = 290K$.

3.2 Domains definition

The model defined in the scope of this study is inspired from a supersonic anti-aircraft missile, the FM-92X "Stinger". Despite being a military weapon, its geometrical characteristics are quite well known and easily accessible online. The fluid and solid domains are defined in the CAD interface of `OOFELIE::Multiphysics`. The fluid domain defined is then transmitted to `FINE™/Open`, where the meshing and the computation of the fluid solution are performed.

3.2.1 Solid domain

The external dimensions of the Stinger missile are based on several online ressources, among which [Mil] and Lyons [Joh12] are the more relevant. The material used for the modelling of the optical window is the same as used for the actual FM-92; a material is extrapolated for the body, having considered the geometrical simplifications performed.

Geometry

The geometry is simplified for the sake of simplicity and feasibility of the model. A first simplification consists in not considering the fins in the model; their influence on the solution only concerns the thermal exchange they do with the flow. Taking account of their small surfaces and since fins become negligible in convective heat transfer at high speed, they are neglected. The internal geometry is reduced to its simpler self, with a uniform, full body considered for the fuselage: information is lost on the actual heat transfer within the body, but the present study aims to present qualitative results. For the same reasons the whole optical sensor system including actuators and cooling devices is not represented. The optical sensor has therefore no physical representation in the FSI model. This quite strong hypothesis ignore any sort of heat transfer from the structure to the sensor, which can be justified by the presence of an argon overcooling system for the actual optical sensor. The head of the missile is therefore represented by an empty dome, which thickness is 3 [mm].

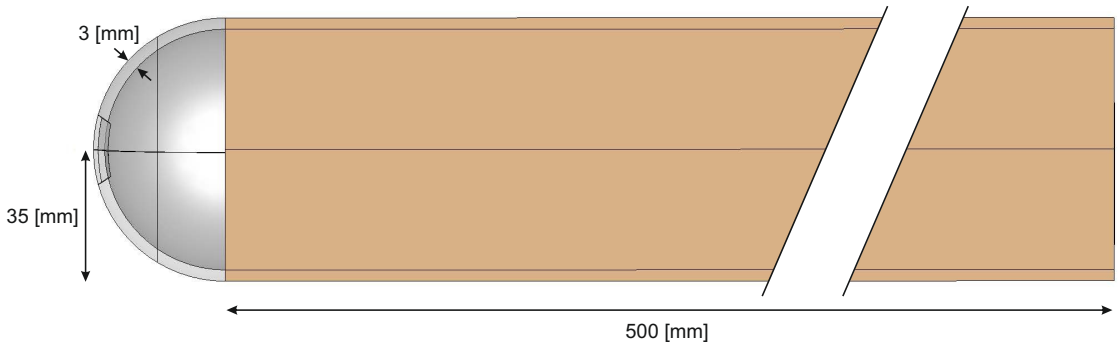

Figure 3.2.1: Sectionnal view of the solid domain.

In order to focus on the region of interest, the solid domain is restricted longitudinally to the head and to a fraction of the fuselage. The part of body considered in the model should be long enough so that the thermal boundary conditions imposed at the bottom are sufficiently far away from the dome; the length considered is 500 [mm], which is nearly 15 times the radius of the optical dome on which the thermal solution matters.

Subdivisions of the domain are performed in order to ensure good mesh quality. The layout of the solid model is represented in Fig. 3.2.1.

Materials

The choice of material for the solid model is particularly important concerning the optical window, since the material properties will define the reaction to temperature, and therefore the variation of index of refraction and thermo-mechanical deformations. The material used is the aluminum oxynitride (ALON), an optical ceramic widely used in military-grade optics. It is actually used in the FM-92. Its relevant properties are (Tab. 3.2.1 from [Sur]) :

Density	ρ	3696	$[\mathrm{kg \cdot m^{-3}}]$
Young's modulus	E	323	[GPa]
Poisson's coefficient	ν	0.24	[-]
Thermal expansion coefficient	β	6.4×10^{-6}	$[K^{-1}]$
Thermal conductivity	k	13	$[\mathrm{W \cdot m^{-1} \cdot K^{-}1}]$
Max. Usable Temperature	T_{max}	1780	[K]

Table 3.2.1: Thermo-mechanical properties of aluminum oxynitride (ALON).

The material attributed to the body is an alloy typically used in missiles structural parts: the X17U4 steel. Its relevant properties are presented in Tab. 3.2.2 from [AD].

Density	ρ	7800	$[\mathrm{kg \cdot m^{-3}}]$
Young's modulus	E	200	[GPa]
Poisson's coefficient	ν	0.3	[-]
Thermal expansion coefficient	β	10.4	$[\mathrm{K^{-1}} \times 10^{-6}]$
Thermal conductivity	k	16	$[\mathrm{W \cdot m^{-1} \cdot K^{-}1}]$

Table 3.2.2: Thermo-mechanical properties of the structural alloy.

3.2.2 Fluid domain

As stated in Sec. 3.1.1, the perturbations due to the body cannot travel upstream; as a consequence the flow upstream the shock wave is the unperturbed freestream. The boundaries of the fluid domain can therefore be defined close to the expected location of the shock, with however a conservative distance. In the present case, the fluid domain dimensions are chosen as a multiple of the body dimensions for the radius, as presented in Fig. 3.2.2. The longitudinal dimension is set to 1 [m].

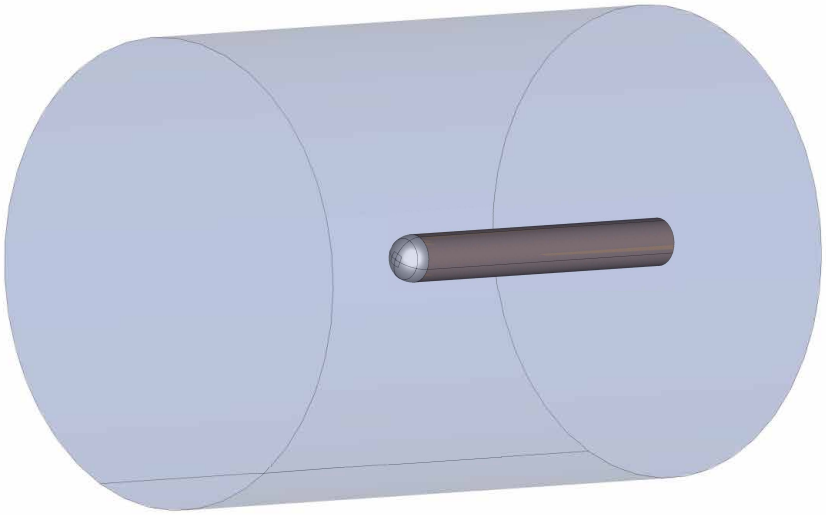

Figure 3.2.2: Representation of the solid and fluid domains.

3.3 Numerical resolution

In order to obtain the solution to the governing equations, these are expressed in terms of finite differences and finite volumes schemes accordingly to a spatial and temporal discretization of their respective domains.

Free stream and thermal conditions are then applied to the boundaries of the domains, defining the solution of the numerical schemes. Several flow configurations are considered for these boundary conditions, comporting variations of the angle of attack of the body in the flow and an increase of the free stream velocity.

The Fluid-Structure Interaction is achieved through communication between the fluid and structural solvers; the thermal coupling between the Solid and Fluid blocks can actually be considered as a type of boundary conditions for the solid and fluid domains. The two solvers in `OOFELIE` and `FINE™/Open` have already proven to provide good quality solutions both separately and conjointly for FSI calculations. In this context studying the dependency of the solution is not relevant, provided that the mesh used are refined and of good quality in the regions of interest.

3.3.1 Boundary conditions & coupling strategy

The boundary conditions on the fluid domain are imposed in FINE™/Open; considering that the missile on which the model is based is a man-portable anti aircraft missile, the temperature and pressure considered are standard conditions at low altitude. The missile quickly reach its maximal velocity, which correspond to $M = 2.5$ in ground conditions. The corresponding velocity is considered as the nominal velocity of the missile.

- The inlet and outlet are defined accordingly to the fluid domain definition; since the flow is supersonic, the outlet boundary conditions are extrapolated from the interior through first order extrapolation.
- The other fluid boundaries are defined in free stream conditions: these are defined in terms of pressure, temperature and velocity components. They are noted with a subscript "A_∞". For the basic case where no angle of attack is considered,
  - $p_\infty = 101325$ [Pa],
  - $T_\infty = 290$ [K],
  - $V_{x,\infty} = 0$ [m/s],
  - $V_{y,\infty} = 0$ [m/s],
  - $V_{z,\infty} = 845$ [m/s] .

Several other sets of boundary conditions are defined, corresponding to other flow configurations:

- For nominal missile speed ($M_\infty = 2.5$), several angles of attack are defined:
  - $\alpha = 0°$,
  - $\alpha = 5°$,
  - $\alpha = 10°$,
  - $\alpha = 20°$.
- A greater missile Mach number is considered, with $M_\infty = 4$.

The boundary conditions on the solid domain are imposed in OOFELIE; they consists in displacement constraint to avoid a rigid body solution, and a thermal condition. The boundary of the solid domain is far away from the shock and the subsequent aerodynamic heating, therefore the body temperature in this location can be estimated to equal the free stream temperature.

Finally, special conditions are defined on the fluid-structure interface. In OOFELIE, FSI panels are defined in order to specify the surfaces of the solid and fluid domains that interact with each other. This topology information is transmitted to FINE™/Open in the form of a *.fsi* file. The thermal coupling strategy consists in an exchange of solutions between the meshes, initiated by the MPI connection between the solvers. These thermal and displacement fields transferred at the interface are considered as a boundary condition for the next iteration. In practice a number of sub-iterations is defined, depending on the presumed strength of the coupling. This procedure is carried on until convergence, i.e. equality of the temperature fields at the interfaces. In the present case the physics are assumed strongly coupled, as the interaction between the two environments is in the two ways: the flow influence the solid solution by defining thermal conditions, but the thermal conditions on the solid may also introduce perturbations and modify the flow solution.

3.3.2 Discretization schemes

The fluid and solid domains are discretized respectively in FINE™/Open and OOFELIE. The general problem is steady, therefore the solution is independent of time. However it is more efficient to solve the set of unstationary equations and let the solution converge to the stationary solution: this is the time-marching approach. Therefore a pseudo time integration scheme is used on each domain.

– Fluid domain

The spatial discretization of the domain is based on an unstructured, cell centered finite volume approach. Considering the finite volume discretization, the conservation laws over a control volume Ω_j writes:

$$\frac{\partial}{\partial t}(U_j\Omega_j) + \sum_{sides}(\mathcal{F}\cdot\mathbf{S}) = 0, \tag{3.3.1}$$

where U is the quantity being conserved, $\mathcal{F}$ is the numerical flux, *sides* refers to the external sides of the volume control and $\mathbf{S}$ is the normal vector to the considered side. The numerical flux can be written in terms of its inviscid and viscous parts: $\mathcal{F} = \mathbf{F} - \mathbf{G}$.

– The viscous fluxes are discretized with a central scheme, the gradients being evaluated directly on the cell faces. Considering a quantity Q, and applying Gauss' theorem over a volume encompassing the considered face:

$$\nabla Q = \frac{1}{\Omega}\int Q\mathbf{ds} = \frac{1}{\Omega}\sum_{l}^{n}{}^{sides} Q_l\mathbf{S}_l \tag{3.3.2}$$

after the finite volume discretization.

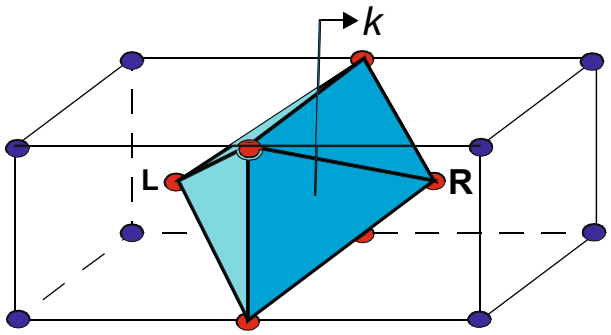

Figure 3.3.1: Diamond control volume for gradient computation on faces.

The theorem is applied on a diamond control volume, as depicted on Fig. 3.3.1; it requires the values of the flow quantities at the cell vertices. These values are obtained from the neighbouring cell centers by a first order interpolation method, such that a quantity Q at a vertex p is obtained from the values at the centers of the surrounding cells Q_i:

$$Q_p = \frac{\sum_{i=0}^{n} Q_i\omega_i}{\sum_{i=0}^{n}\omega_i} \tag{3.3.3}$$

with ω_i the weighting functions defined as

$$\omega_i = 1 + \lambda_x \Delta x_i + \lambda_y \Delta y_i + \lambda_z \Delta z_i. \tag{3.3.4}$$

Δx_i, Δy_i and Δz_i are the coordinates difference between the vertex p and the cell center i. The weighting coefficients λ_x, λ_y and λ_z are determined by enforcing the first order interpolation. A more complete development is available in annex A.2.

–The inviscid fluxes across a face are expressed as

- the average of the inviscid fluxes at the centers of the bounding cells for the internal faces:

$$(\mathbf{F}\cdot\mathbf{n})_k = \frac{1}{2}\big((\mathbf{F}\cdot\mathbf{n})_R + (\mathbf{F}\cdot\mathbf{n})_L\big) - \frac{1}{2}d_k. \tag{3.3.5}$$

- a flux based on averaged unknowns on the boundary faces:

$$(\mathbf{F}\cdot\mathbf{n})_k = \mathbf{F}\Big(\frac{U_L + U_R}{2}\Big)\cdot\mathbf{n} - \frac{1}{2}d_k \tag{3.3.6}$$

with d_k a numerical dissipation term.

This numerical dissipation term is formulated as established by Jameson, Schmidt and Turkel ([Ant17]): a blend of first and second order differences of the conservative variables.

$$d_k = \epsilon_k^{(2)}\delta U_k + \epsilon_R^{(4)}\delta^2 U_R + \epsilon_L^{(4)}\delta^2 U_L, \tag{3.3.7}$$

with

- δU_k is the first order difference in face k,
- $\delta^2 U_R$ and $\delta^2 U_L$ are the second order differences in the left and right cell centers,
- $\epsilon_k^{(2)}$ and $\epsilon_k^{(4)}$ are second and fourth order coefficients in face,
- $\epsilon_R^{(4)}$ and $\epsilon_L^{(4)}$ are fourth order coefficients in cells. These are obtained by arithmetic averaging of the fourth order coefficients on the constitutive faces of opposite sides.

The non dimensional coefficients v_L and v_R are defined as temperature and pressure variations:

$$\text{For instance,} \qquad v_L = \max\left\{\frac{|p_{L+1} - 2p_L + p_{L-1}|}{|p_{L+1} + 2p_L + p_{L-1}|}, \frac{|T_{L+1} - 2T_L + T_{L-1}|}{|T_{L+1} + 2T_L + T_{L-1}|}\right\}, \tag{3.3.8}$$

where p_{L-1} is the averaged pressure over the cells located at the left side of cell L in the considered direction (determined by the face k). They act as sensors in order to detect the presence of strong gradients or discontinuities, as it is the case in the presence of a shock wave. This allows to activate the second order term of the dissipation expression in regions of strong gradients, therefore reducing the scheme order at discontinuities. As a consequence the numerical oscillations appearing at strong discontinuities are mititgated.

The pseudo time integration is performed using a multistage Runge-Kutta scheme, accelerated by a multigrid technique. For the general formulation of the time integration problem $dfracdUdt = F(U)$, the explicit 4-stage Runge-Kutta as used in FINE™/Open can be written:

$$\begin{aligned} U^{(1)} &= U^n + 0.25\Delta t F(U^n) \\ U^{(2)} &= U^n + 0.333\Delta t F(U^{(1)}) \\ U^{(3)} &= U^n + 0.5\Delta t F(U^{(2)}) \\ U^{(4)} &= U^n + \Delta t F(U^{(3)}) \\ U^{n+1} &= U^q \end{aligned} \tag{3.3.9}$$

The multigrid strategy consists in damping the low frequency errors that decrease very slowly by transferring the solution on a coarser grid, in which such errors manifest themselves as higher frequency errors. This sequence can be repeated recursively on a hierarchy of coarser grids, responsible for eliminating particular bandwidth of errors. The solution is then transferred back on the fine grid. In the present case, 4 grid levels are used, organized in a "V-cycle". 200 temporal iterations are performed at each grid level.

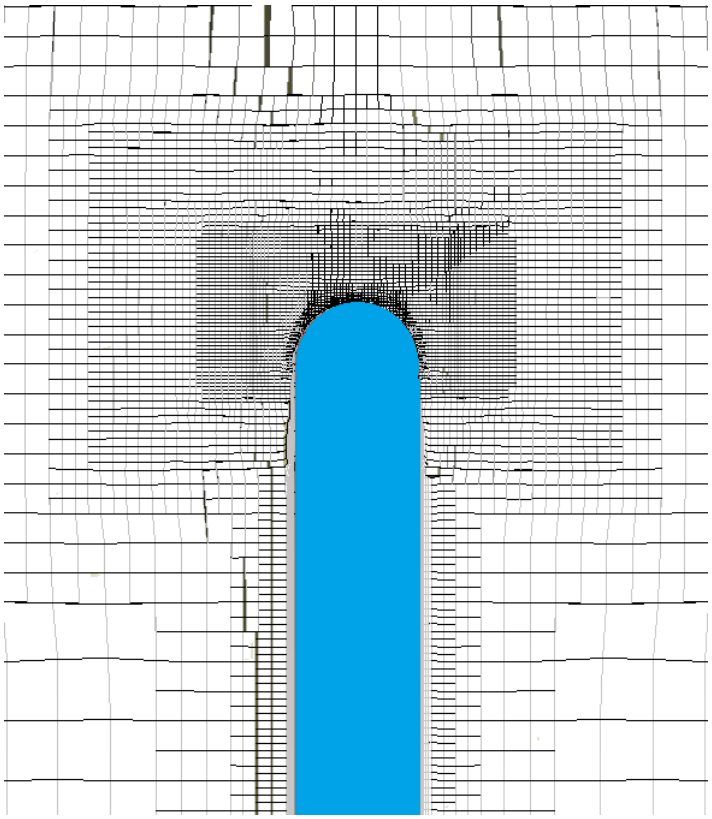

Figure 3.3.2: View of the unstructured spatial discretization used for the FSI simulations.

An adaptation of the mesh at proximity of the wall is also performed, in order to refine the mesh inside the boundary layer region. The mesh in this region is semi-structured in order to limit the number of hanging vertices in the streamwise direction near the wall. The mesh in the vicinity of the this region is also modified in order to provide a smooth stretching progression (ratio = 1.2) from the wall layer to the outer layer.

In practice, the discretization is performed by a nearly automatic all-hexahedra unstructured meshing procedure available in the `HEXPRESS` software (integrated in `FINE™/Open`). The unstructured approach allows to refine efficiently the mesh in the region of interest - in this case the proximity of the optical window and the region where the shock is expected. This zone is estimated from the empirical formula for shock waves over blunt bodies: Equ. 3.1.15. As a result, less elements are necessary while obtaining a satisfactory element size in the area of interest: the mesh used for the simulations (Fig. 3.3.2) is composed of 700 000 cells, with 5 [mm] side length elements in the area of interest and 3 [mm] in the vicinity of the solid surface.

– Solid domain

The solid domain is discretized in finite elements by the `Samcef Field` mesher embed in `OOFELIE`. A mapping of the optical window is performed in order to ensure a good mesh quality in this critical region, resulting in the mesh presented in Fig.3.3.3. The width of the optical window is discretized by 3 elements.

The mesh consists in 107840 elements, 98% of which are quadratic hexahedrons; the remaining ones are quadratic pentahedrons. The mean element size on the optical window is 1.5 [mm].

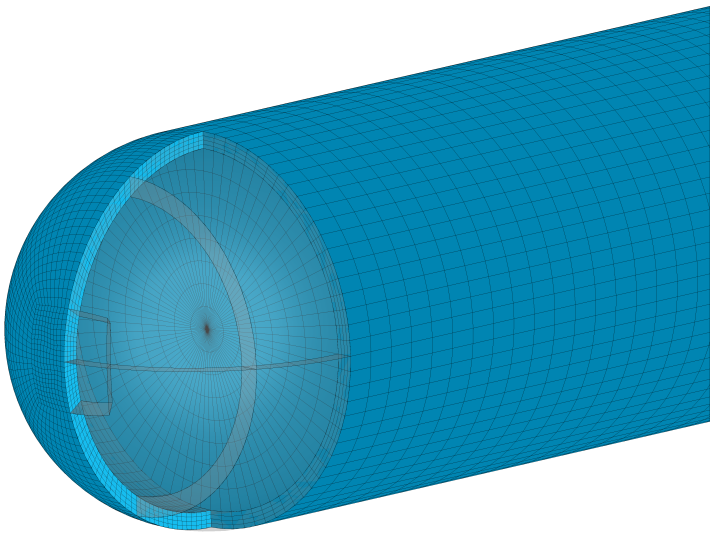

Figure 3.3.3: Display of the finite element mesh on the optical window.

The pseudo temporal integration of the discretized thermo-elastic equations is performed by a Hilbert-Hughes-Taylor (HHT) method.

3.4 Fluid and structure solutions

Several set of boundary conditions were defined in Sec. 3.3.1, corresponding to different flow configurations. The results corresponding to the cases of $\alpha = 0°$, $\alpha = 20°$and $M_\infty = 4$ are displayed in the following figures.

The increase of the flow quantities through the shock wave is clearly visible, with a noticeable weakening of the shock as the flow is further from the body, as predicted by the theory. Note that at approximately one diameter from the body, the shock appears much less sharp and seems evanescent: although the shock strength decreases quickly, this phenomenon is mainly due to the increasing mesh size. This location is considered out of the region of interest, and the mesh was defined coarse in this region, as shown in Fig. 3.3.2. This has a damping effect on the obtained solution of the shock, which is not reliable out of the refined region. However the flow being supersonic, the good solution in the region of interest is not affected by the spurious solutions generated outside.

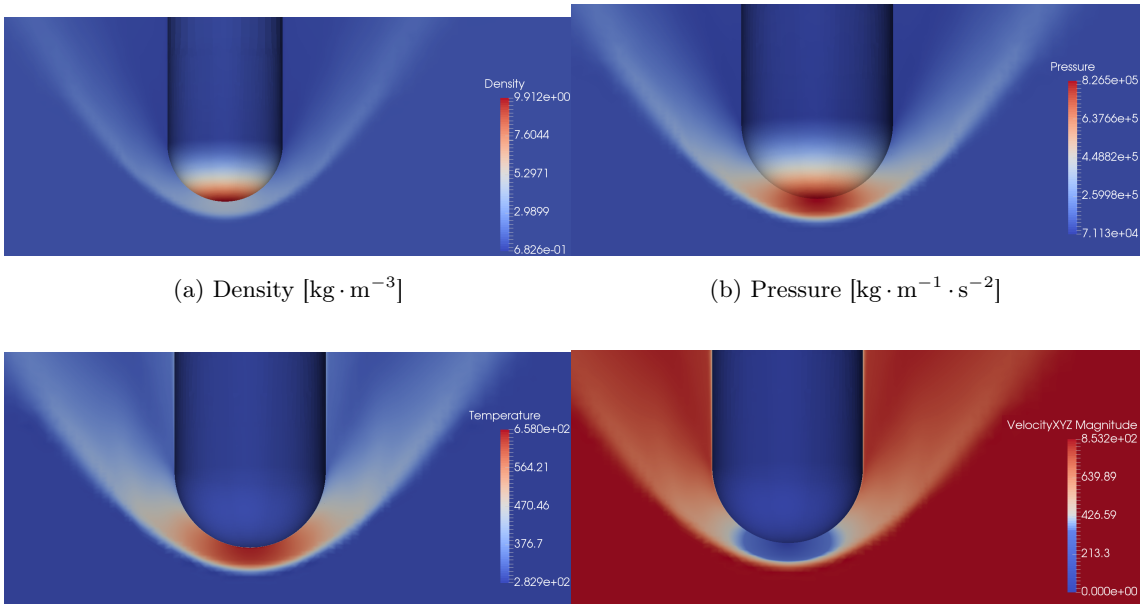

(a) Density [$\mathrm{kg \cdot m^{-3}}$]

(b) Pressure [$\mathrm{kg \cdot m^{-1} \cdot s^{-2}}$]

(c) Temperature [K]

(d) Velocity magnitude [$\mathrm{m \cdot s^{-1}}$]

Figure 3.4.1: Main flow quantities in the case of a 0 °angle of attack of the body.

As observed in Fig. 3.4.1d and 3.4.2d, the subsonic region predicted in Sec. 3.1.1 is present behind the part of the shock that is normal to the freestream. The other flow quantities behind the shock wave are concording with what is expected from the Rankine-Hugoniot jump relations; another effect that could not be quantified in Sec. 3.1 is the compression of the air in the subsonic region, which further increases the pressure, density and temperature.

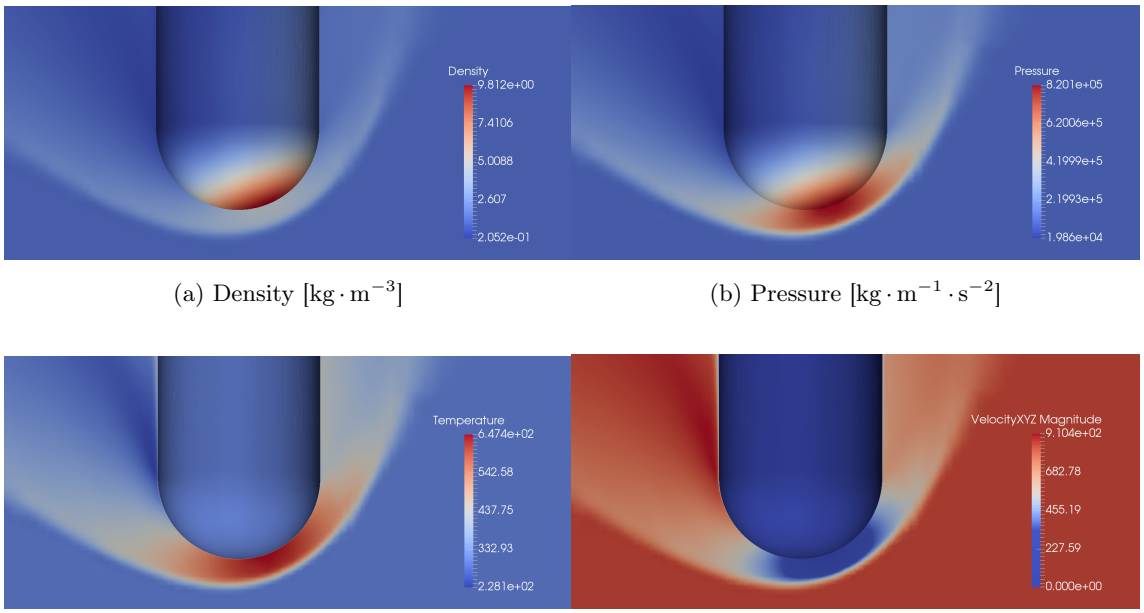

(a) Density [$\mathrm{kg \cdot m^{-3}}$] (b) Pressure [$\mathrm{kg \cdot m^{-1} \cdot s^{-2}}$]

(c) Temperature [K] (d) Velocity amplitude [$\mathrm{m \cdot s^{-1}}$]

Figure 3.4.2: Main flow quantities in the case of a 20 °angle of attack of the body.

Another interesting phenomenon takes place in the results, particularly visible in the case of an angle of attack of 20 °: it appears that a part of the flow accelerates when passing by the end of the optical dome; simultaneously the temperature, pressure and density decrease. This is the effect of expansion waves through which the flow is continuously deflected so that it remains tangential to the surface of the body. However the results in this region must be taken with care: there could be other phenomena -such as interactions with the boundary layer- that are not or badly represented due to the roughness of the mesh in this region. However this does not occurs in the region of interest nor influences the flow near the optical window.

The temperature of the flow in front of the body increases abruptly due to the shock wave and the isentropic compression of the flow. As a consequence, the temperature of the structure increases as well, particularly in the vicinity of the stagnation point. As shown respectively on Fig. 3.4.4 and 3.4.5, the temperature of the dome and of the structure increased considerably, particularly at the stagnation point. Note that in the flow configuration where a Mach number equal to 4 is considered, the temperature of the dome rises up to 1220 [K]; this peak value is however still below the maximal operating temperature of the ALON (cf Tab. 3.2.1).

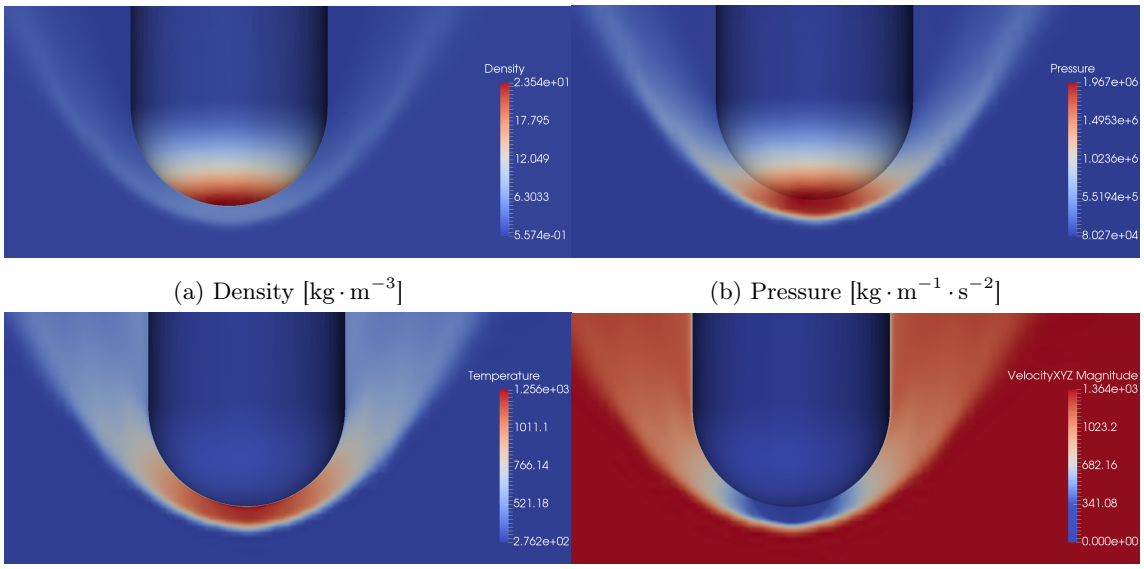

(a) Density [$\mathrm{kg} \cdot \mathrm{m}^{-3}$] (b) Pressure [$\mathrm{kg} \cdot \mathrm{m}^{-1} \cdot \mathrm{s}^{-2}$]

(c) Temperature [K] (d) Velocity amplitude [$\mathrm{m} \cdot \mathrm{s}^{-1}$]

Figure 3.4.3: Main flow quantities in the case of a free stream Mach number equal to 4, $\alpha = 0$.

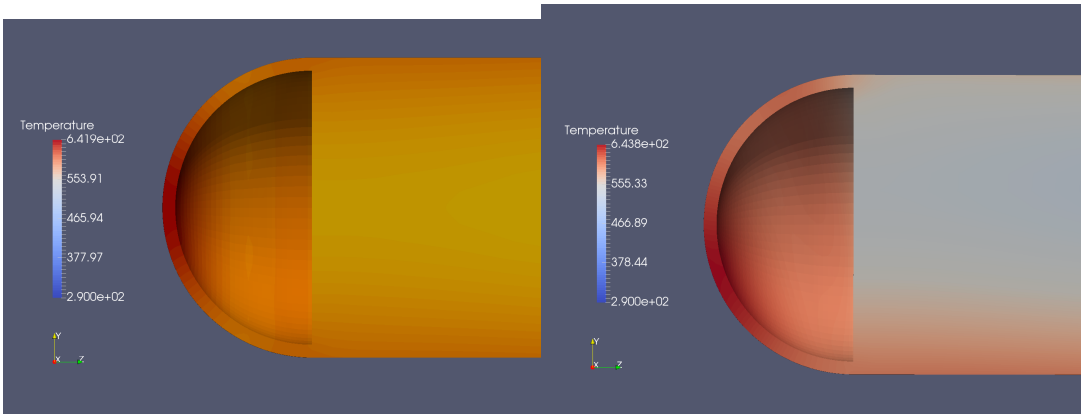

(a) α=0° (b) $\alpha = 20°$

Figure 3.4.4: Temperature field of the body and of the optical dome, in the flow configuration where $M = 2.5$.

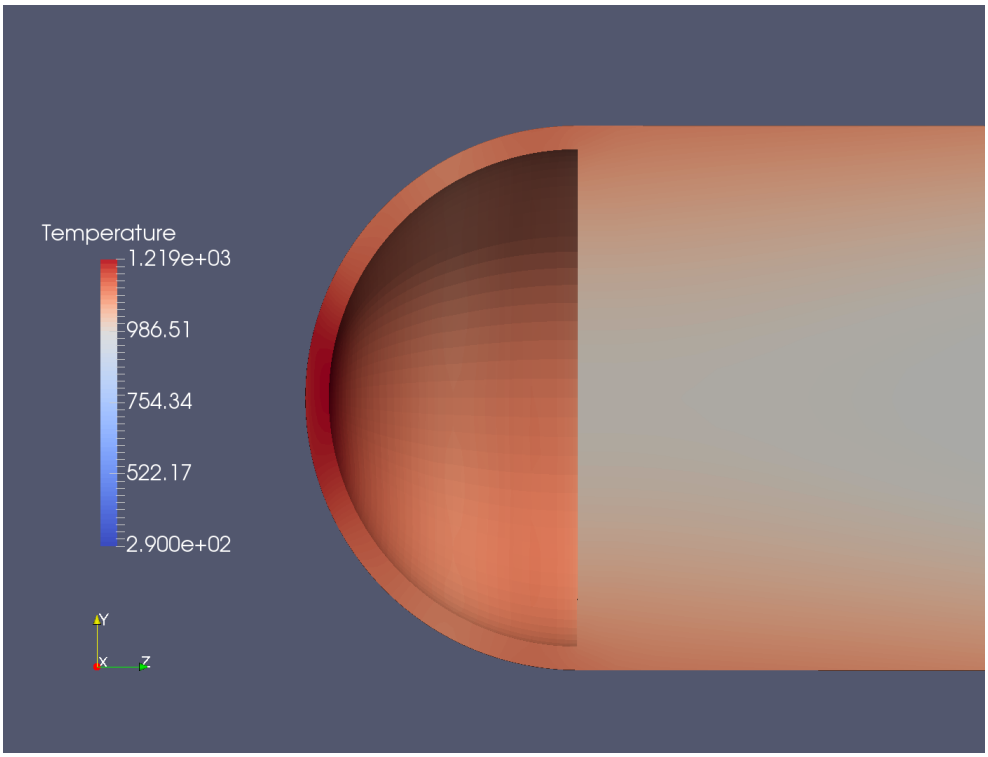

Figure 3.4.5: Temperature field of the body and of the optical dome, in a flow configuration corresponding to an angle $\alpha = 0°$and $M = 4$.

Chapter 4

Intermediary processing of the fluid results

As it was depicted in Fig. 2.0.1, the processing of the results takes place after the fluid-structure interaction computation. The processing operations aim to provide usable data to the optical modelling software, i.e. transmit in the appropriate format the data relative to the identified optical disturbances sources.

Once the FSI solutions obtained, the operations to be performed are the following:

- transmit the thermal field on the optical window in order to compute $GRIN_{window}$,
- transmit the deformation field of the optical window,
- transfer the fluid solution from the unstructured fluid mesh to an interpolation mesh,
- detect the shock wave and provide a characterization of the shock surface,
- determine and transmit a subset of nodes of interest representing the perturbed region of the flow, in order to define GRIN_{air}.

The two last procedures are developed as a part of the present work and constitute a personal contribution to the workflow.

The post processing being in development, it is not yet integrated in a continuous workflow. Instead data are transferred by differed transmission: the results are written in dedicated files, which are then specified in the input of the following procedure.

4.1 Transfer of the fluid solution on the interpolation mesh

In most Fluid-Structure Interactions applications, only the flow fields at the interface are of interest and are transmitted by default to `OOFELIE`, the whole flow solution still being available for visualization in the `FINE™/Open` viewer interface. Due to the prevalent use of parallel computing in fluid solvers, the solution is fragmented into each of the processors computations. Moreover, `OOFELIE` can not handle the solution exported on the fluid mesh due to its unstructured topology: `OOFELIE`

has not the tool to represent the presence of hanging nodes. A new structure is therefore required to perform operations on the solution, possibly for other applications that the present work. The mesh transfer procedure accesses successively the solutions from each processor and transfers them by interpolation on a mesh defined in `OOFELIE`. The solution is therefore defragmented on a mesh whose topology is fully accessible and controlled. In order to speed up the transfer procedure, the interpolation mesh is defined such that it is well refined in the region of interest, while being coarse in areas where the solution is not used anyway.

4.1.1 Interpolation method

The interpolation method is based on the identification of the fluid cell in which each node of the interpolation mesh is located. The flow quantities at the node are then interpolated from the values at the cell vertices.

The localization of the current node of the interpolation mesh (called n_{int} in the following) in the fluid mesh is based on the following method:

0. The fluid domain is subdivided by planes that do not pass through the fluid nodes, such that each fluid node is enclosed in an individual "box".
1. Using the "bounding box" of the fluid domain, defined by the knowledge of the extremal planes (in bold in Fig. 4.1.1), the box in which n_{int} is located is identified by dichotomy. This step imply a number of operations of the order $\sim \log_2 n$.
2. The fluid cells intersected by the planes defining the box found previously are identified. These are the cells that potentially contain n_{int}.
3. The location of n_{int} is finally obtained by comparing its coordinates with those of the reduced set of cells.

The method is represented in Fig. 4.1.1 on a 2D case to ease the comprehension and the readability of the operations.

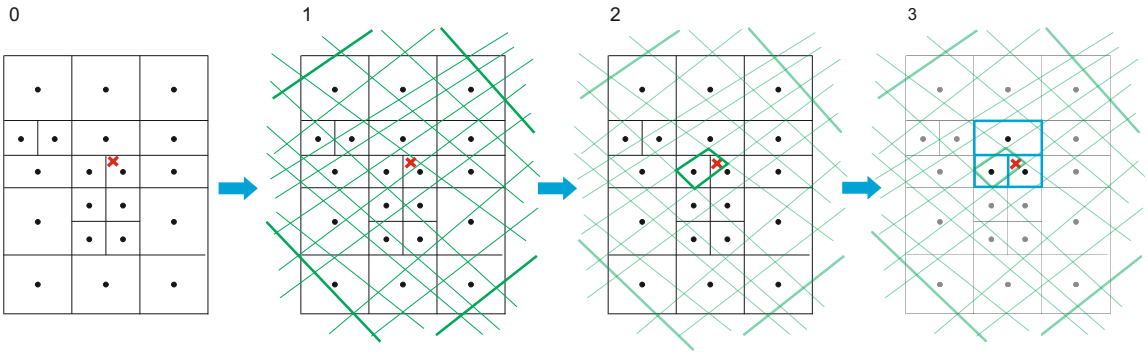

Figure 4.1.1: Representation of the localization process of a node of the interpolation mesh into the cell of the fluid mesh.

Finally, the flow quantities at n_{int} are interpolated to the first order from the values at the vertices of the fluid cell. The method is efficient in terms of computational cost: it implies a total number of operations of the order of $n \log_2 n$.

4.1.2 Interpolation mesh used

The creation of the interpolation mesh is performed in `OOFELIE`. Its definition is critical since it directly determines the mean distance between the nodes in the region of interest. This parameter influences most of the subsequent processing operations, and basically defines the number of nodes used for the computation of $GRIN_{air}$. The interpolation mesh should therefore be well refined in the region where the shock takes place, and in which the nodes will be selected for the computation of the gradient of index. The domain used to support the interpolation mesh is subdivided several times in order to optimize the distribution of the nodes: a lot of nodes can be placed in the region of the shock and optical window, with on the other hand a low node density elsewhere in the flow. The target element size in the region of interest is fixed to 2 [mm]; in practice the obtained mean distance between the nodes is computed equal to 3 [mm]

Another important mesh parameter to discuss is the type of elements used in the interpolation mesh. The elements themselves are not used to perform the interpolation, i.e. their shape or "quality" as finite elements does not matter in the present case. However their nature defines the way the nodes are arranged in the domain. At this stage of development, the interpolation method works with 1^{st} order elements only. Two approaches are considered:

- a structured mesh composed of hexahedrons arranged by LUI mapping, as shown on Fig. 4.1.2,
- a fully unstructured mesh composed of tetrahedrons, as shown on Fig. 4.1.3.

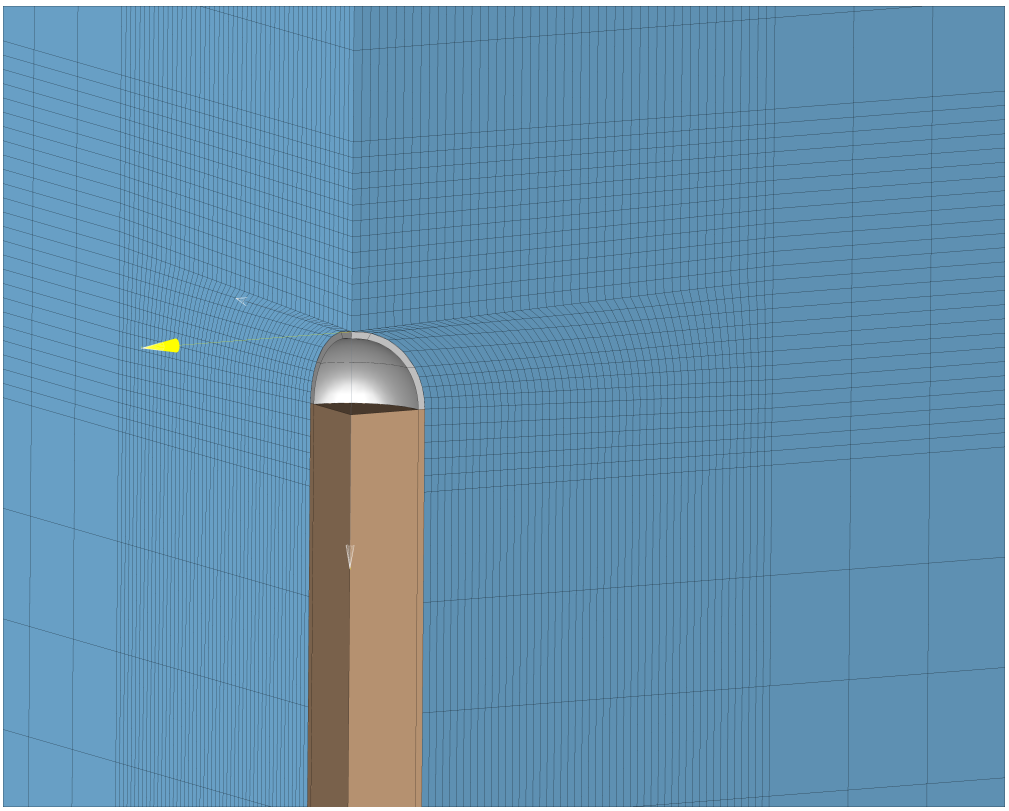

Figure 4.1.2: Sectional view of the structured interpolation mesh composed of mapped hexahedrons.

At first, a highly structured mesh might appear to be a good candidate: the regularity of the disposition of the nodes allows to simplify several steps of the processing procedures. However,

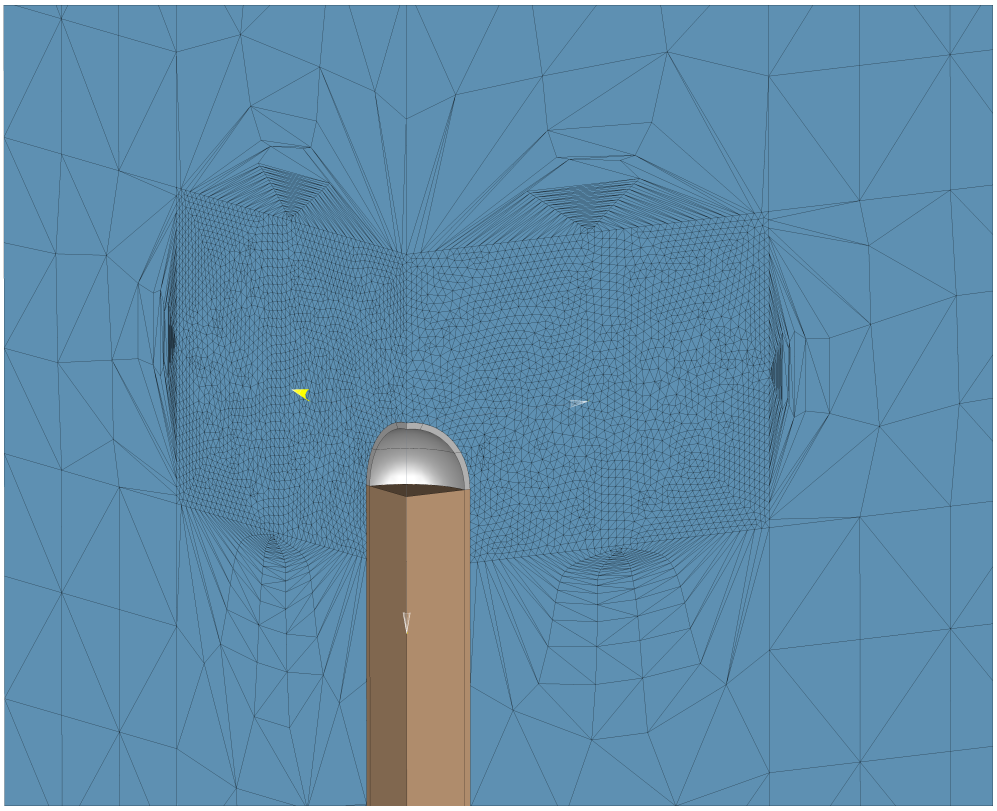

Figure 4.1.3: Sectional view of the unstructured mesh composed of tetrahedrons.

the mesh is regular along directions fixed to the body; in practice this decrease the effectiveness of shock wave detection in the case where the flow solution is not aligned with the mesh. (i.e. in case of an angle of attack of the body). Moreover in the present case the regularity of the mesh introduces an axial symmetry of the nodes disposition. This skews the shock detection and shock shape characterization: since the nodes are arranged in symmetrical patterns, these patterns are found again in the set of nodes constituting the shock. This bias can be avoided by using an unstructured mesh: in this case the eventual symmetry of the solution found is not enforced by the node distribution.

Finally the use of a regular mesh require to impose the same number of elements on the faces of each sub-domains in one direction; this reduces the efficiency of the sub-division with the creation of a lot of very thin elements out of the region of interest. As compared in Fig. 4.1.4, the unstructured tetrahedic mesh allows a higher proportion of nodes in the region of interest.

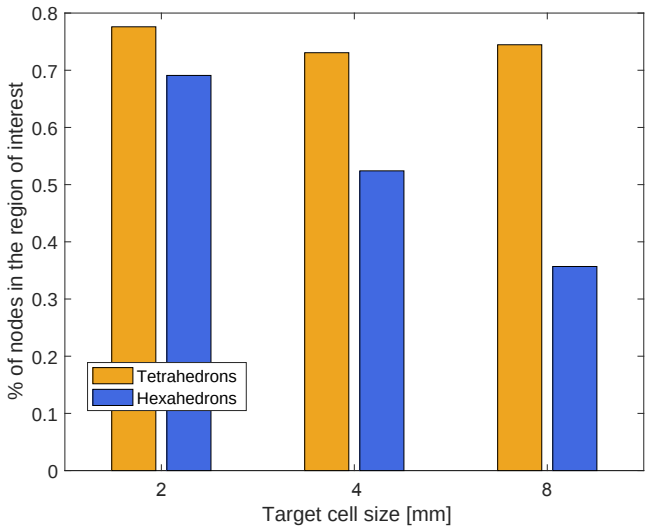

Figure 4.1.4: Comparison of the percentage of nodes located in the region of interest, depending on the type of mesh and mesh elements used.

As a more practical consideration, the tetrahedric meshing is fully automated and is very flexible. On the contrary producing a structured mesh of hexahedrons may require a lot more of work.

4.2 Detection and characterization of the shock wave

As established previously, the flow upstream the shock is undisturbed. It is therefore of prime interest to localize the shock wave: this allows to determine the portion of the flow that is perturbed, and in which variations of temperature, pressure and density define the near-field optical disturbances.

Before the proceedings, the domain of research can be reduced by taking consideration of the estimated stand off distance of the shock Δ_0 from Sec.3.1.1. Under the considered conditions, $\Delta_0 = 8.5$ [mm]. Moreover the portion of the shock downstream of the optical window is not of interest in the present case; this defines a second longitudinal boundary. Radially, the domain of research is restricted to 1.5 times the diameter of the solid body, which correspond to a margin of 30% of the distance of the shock at the end of the optical window, as estimated by the empirical formula Equ. 3.1.15.

The problem of shock detection is to be addressed theoretically and practically, considering that the flow quantities are available in discrete locations. The level of characterization of the shock is of prime importance in terms of the computation of the related optical effects: as developed later in Sec. 5.1, the ray deviation caused by a gradient of refractive index depends on the orientation

of this gradient. In the case of the shock, the gradients are normal to its surface; therefore an erroneous surface definition introduces errors in the optical modelling.

Characterizing the shock surface by an analytical expression is appealing: the normal to the surface in any point can be directly obtained from the implicit formulation $F(x, y, z) = 0$, with $\mathbf{n}(x, y, z) = \nabla F(x, y, z)$. This expression has only to derived one time ("by hand" by the user or derived numerically). In order to obtain the analytical expression of the surface from the discrete points where the shock is detected, a least squares error parameter fitting is performed for different types of surface functional.

4.2.1 Shock nodes detection

Historically a lot of shock detection techniques have been developed, based on different theoretical characteristics of the shock wave and of the supersonic flow.

The most basic techniques are based on the construction of isovalues surfaces of flow quantities. Due to the variation of the flow quantities through the shock, an isosurface of a flow quantity slightly above the free stream value can be found in the shock wave. Obtaining the shock surface is straightforward, however it relies on vizualisation of the flow and selection of the adequate isosurface. Moreover only a part of the surface obtained corresponds to the shock and is of interest, it must therefore be separated manually. As a result the method provides rather good results quickly, but it requires multiple user interventions and an additional post processing to obtain an analytical expression of the surface; as such it is not suitable for a chained workflow.

The shock detection based on the method of characteristics is probably the most advanced to this day: as presented in [KS13], the 3D implementation provides good results even in complex configurations (f.e. shock interactions) and is extendable for the detection of moving shock waves. However its high computational cost and especially the complexity of the implementation of the method makes it unattractive for the present application.

In terms of computational and implementation costs, an intermediary family of methods is based on the detection of the jump of the flow quantities across the shock. In the conventional implementation, a shock is considered to occur between two adjacent nodes if the gradient of one or several flow quantities is high between these nodes. This requires the definition of an adapted criteria which acts as a filter to sort shock-related gradients apart from the other variations of flow quantities. However the choice of a good filter parameter might become challenging since it is dependent on both the flow conditions and the spatial discretization. In the present work, a workaround to such specific criterion is developed by using the Rankine-Hugoniot jump relations in terms of the Mach number (Equ. 3.1.10 to 3.1.13).

Indeed as stated in Sec. 3.1.1 the bow shock starts as a normal shock and turns into increasingly leaning oblique shocks far away from the body; it eventually evolves into a Mach wave. Therefore a range of flow quantities variations is defined, from the normal shock to the Mach wave; in practice since the flow quantities do no vary through a Mach wave, a slightly greater angle is considered. The shock detection criteria is therefore based on the flow quantities variations associated to this "lower bound" angle: a shock is considered to occur between two nodes if the pressure and density variations (defined by Equ. 3.1.12 and Equ. 3.1.11) are greater than the variations due to a shock of angle $\mu + \Delta\beta$, with

- μ the Mach angle,
- $\Delta\beta$ the increase of shock angle such that the criterion is greater than 1. This parameter basically defines the region of the shock that is detected; in practice an increase of angle of 5° has shown good results.

Several approaches exists for selecting the nodes between which the criterion of detection is applied: the most widely method is applying the criterion between a node and its nearest neighbours. The determination of these close neighbours is computationally heavy if taken in "naive" approach: it typically scales as $O(n^2)$ in time. A more efficient approach can be developed, resulting from the following observations:

- the application of the detection criterion between a node and its neighbours in all directions is redundant,
- the surface of the shock in the region of interest presents a large angle with the freestream direction.

The developed algorithm sorts the nodes by ordered slices of approximately same longitudinal coordinates (along the z axis). The detection criteria is then applied between a node of the current ply and nodes of the next ply that are within a proximity criterion Δ_{max}, which is fixed to a multiple of the mean mesh size. Therefore the node selection is directed towards the flow propagation and limited in distance, defining a pyramidal volume of research as shown in Fig. 4.2.1. The sorting of the nodes is performed by a Bucket sort, which has been proven to be very efficient ([FS17]). The overall procedure scales as $O(n \log n)$ at worst, but in the case of data uniformly distributed over a range such as the z coordinates, it behaves quasi linearly ($O(n)$ at best).

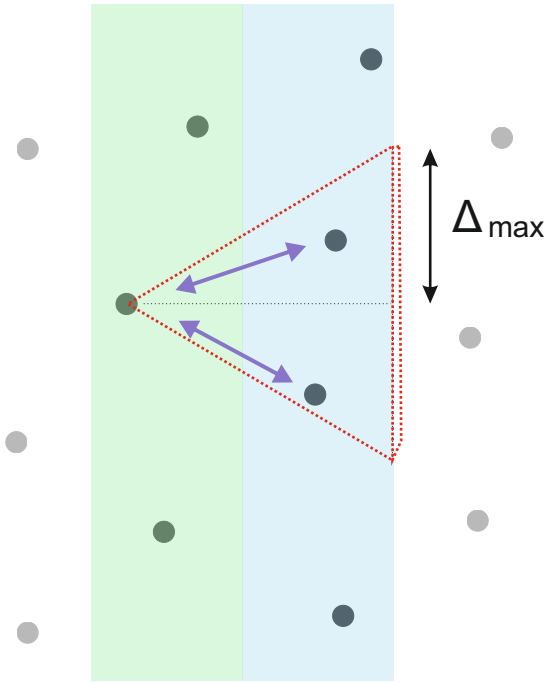

Figure 4.2.1: Representation of the "layers" or "ply" approach for selecting the nodes between which the detection criterion is applied.

The shock coordinates are determined as follows: if a shock is detected between two nodes, the shock node is defined as the median point. The error on the localization of the shock is therefore

equal to half the distance between the nodes. A consequence of this scaling of the error with the distance between the nodes is that the detection of the shock should be restricted to a region where the interpolation mesh was defined well refined. Considering a mean mesh size of the interpolation mesh of 3 [mm] in the region of interest, the error on the location of the shock nodes is therefore less or equal to 1.5 [mm]. The shock coordinates obtained appears to form a coherent surface and are consistent with the results obtained from the visualization of the flow solution: the shock is symmetric, of apparent circular section, and its edge is located at approximately 10 [mm] from the tip of the solid body.

4.2.2 Parameter fitting of the surface

In order to provide an analytical expression of the shock surface, a parametric functional can be fitted to the least square error to the shock nodes obtained previously.

The least squares fitting problem consists in adjusting the parameters $\boldsymbol{\beta}$ of a model function $f(x, y, \boldsymbol{\beta})$ in order to fit the data set of n points: (x_i, y_i, z_i), $i = 1, ..., n$. The optimal parameters are found by minimising the sum of the squared residuals:

$$LSE = \sum_{i=1}^{n} \big(z_i - f(x_i, y_i, \boldsymbol{\beta})\big)^2 \tag{4.2.1}$$

If the function model is a linear combination of the parameters, the residuals can be expressed in the following matricial form: $\boldsymbol{A\beta} = \boldsymbol{z}$. As demonstrated by Strang in [Str06], the unique solution is

$$\boldsymbol{\beta} = (\boldsymbol{A^T A})^{-1} \boldsymbol{A^T z} \tag{4.2.2}$$

In the case of a non linear combination however, there is no closed-form solution; numerical schemes must be applied to find the parameters $\boldsymbol{\beta}$ minimizing the objective function Equ. 4.2.1. A lot of algorithms have been developed to solve the non-linear optimization problem. Two of the most famous are the method of moving assymptots ("MMA", presented by Svenberg in [Sva87]) and the Levenberg-Marquart algorithm; they are robust and efficient, and guidelines for their implementation are easy of access. However the minimization of a non linear expression of Equ. 4.2.1 is computationally costly and might present convergence issues; in particular special attention should be given to the initial set of parameters provided in input. A non linear parametric function is therefore conceivable, but it should present a noticeable improvement of the fitting quality compared to a linear function.

The quality of the parameter fitting can be estimated mathematically by the mean absolute error: it allows to quantify for each function model the average error committed between the fitting function and the set of nodes where the shock was detected. It is formulated as follows:

$$MAE = \frac{1}{n} \sum_{i=1}^{n} \mid z_i - f(x_i, y_i, \boldsymbol{\beta}) \mid \tag{4.2.3}$$

Another indicator frequently used to measure the difference between the values predicted by a model and the actual values is the Root Mean Square Error (RMSE). It is a good measure of accuracy to compare different models in terms of the fitting error; the data can be normalized by

the standard deviation of the data along z. The corresponding expression is:

$$NRMSE = \frac{100}{\sigma_z^2}\sqrt{\frac{1}{n}\sum_{i=1}^{n}\big(z_i - f(x_i, y_i, \boldsymbol{\beta})\big)^2} \tag{4.2.4}$$

The choice of the function model that is used in the least squares parameter fitting is particularly critical: a misfit model will not be able to provide a good fitting of the data. Moreover, whether the formulation is linear or non linear has its importance in terms of resolution of the least squares problem. Finally the function model should be able to represent non symmetrical surfaces, considering that the shock shape is expected to be no longer axisymmetric when the body presents an angle of attack with the flow (see Fig. 3.4.2d).

The `Zemax` standard surfaces library contains a whole set of function models in order to define lens surfaces. Most of them are conics, which imply that they are non-linear and axisymmetrical. An asymmetrical deformation can however be provided by addition of polynomial deformation terms. A promising function model is the biconic surface with polynomial correction: two different curvatures are already available initially, and the polynomial terms allow a good variability of the obtained shape. Its expression is:

$$z = \frac{c_x x^2 + c_y y^2}{1 + \sqrt{1 - (1 + k_x)c_x^2 x^2 - (1 + k_y)c_y^2 y^2}} + \sum_{i=0}^{r}\sum_{j=0}^{s}\alpha_{ij}x^i y^j, \tag{4.2.5}$$

where

- $c = \dfrac{1}{R}$ with R the radius of curvature in the direction specified,
- k is the conicity constant in the considered direction x or y,
- s and r are respectively the maximum order of the polynomial in x and y.

A purely polynomial surface is also considered: since it writes as a linear combination of polynomial terms with parameters α_{ij}, the solution of the least squares problem can be obtained directly by Equ. 4.2.2. The function models considered for the fitting are therefore the following:

- The pure biconic surface,
- The biconic surface with polynomial correction, $r = s = 5$,
- Polynomial surfaces considered at degree 4, 5 and 6.

In order to investigate the adequate choice of surface model, the parameter fitting is first performed in the `Matlab` environment. The comparison between the fitting functions is based on the mean absolute error and the NRMSE. In order to assess the ability of the fitting function to represent different shock configurations, two test cases corresponding to a 0 and 20 °angle of attack are considered.

As presented in Tab. 4.2.1, all the functions get to fit the shock nodes set with a good correspondence according to the NRMSE obtained, at the exception of the 6^{th} order polynomial which presents both a higher indicator value and a higher mean absolute error. This increase of the error of interpolation is a well known issue with high order polynomials, known as Runge's phenomenon. This function is therefore to be disregarded.

	$\alpha = 0$		$\alpha = 20$	
Function	NRMSE	MAE [mm]	NRMSE	MAE [mm]
Biconic	2.39	1.84	3.23	2.06
Biconic + order 5 polynomial	2.38	1.83	3.1	1.96
degree 4 polynomial	2.38	1.84	2.74	2.07
degree 5 polynomial	2.38	1.83	2.74	2.07
degree 6 polynomial	8.36	7.12	7.66	5.9

Table 4.2.1: Computed values of the indicator of fitting quality (NRMSE) and mean absolute error (MAE) for the different functions in the case of an angle of attack of 0 and 20 °.

The yellow highlighting concerns the effective fitting of the biconic-based function for the data of the angle of 20°. Indeed, the non linear minimizer was not able to obtain a solution to the non-linear minimization problem, despite initial conditions defining the surface very close to the data set. This is due to the very definition of the biconic surface, which can not define a tilted surface about x or y. For the second biconic function including polynomial terms, the minimization process tends to delete the biconic term, resulting in a solution similar to the degree 5 polynomial function. A solution to this issue is to define a rotation of the system of coordinates about an angle θ, θ becoming a parameter of the function newly defined. However, the introduction of this rotation of the system of coordinates greatly increases the non linear behaviour of the equation, and makes the resolution unstable. The solution was obtainable only by defining initial conditions such that the surface defined is already close to the data set, including in terms of the tilt angle θ. This reduces the interest of obtaining such solution, since it requires a initial set of parameters already close to the solution.

The use of the biconic surface as a function for the fitting of the shock presents several important drawbacks: not only it requires the use of a non-linear minimization algorithm in order to solve the least squares problem, but the surface is not suitable to represent tilted shocks. Moreover, the quality of fitting does not differ substantially from the ones obtained by polynomial surfaces, which would justify the cost of using a non-linear function.

On the contrary the polynomial surfaces of degrees 4 and 5 show good fitting qualities and good flexibility to the case. Moreover the solution to the least squares problem can be obtained directly by Equ. 4.2.2, which simplify greatly the implementation and ease the integration of the surface fitting in a continuous workflow. The polynomial surface of degree 4 is therefore selected for the shock surface fitting: one additional degree adds six terms in the expression while not showing any improvement of the fitting quality.

A visualization of the obtained surface conjointly to the flow solution in Fig. 4.2.2 shows that the shock surface is indeed well detected and approximated in the different flow configurations. The standoff distance from the body is $\Delta_{num} = 10.44$ [mm].

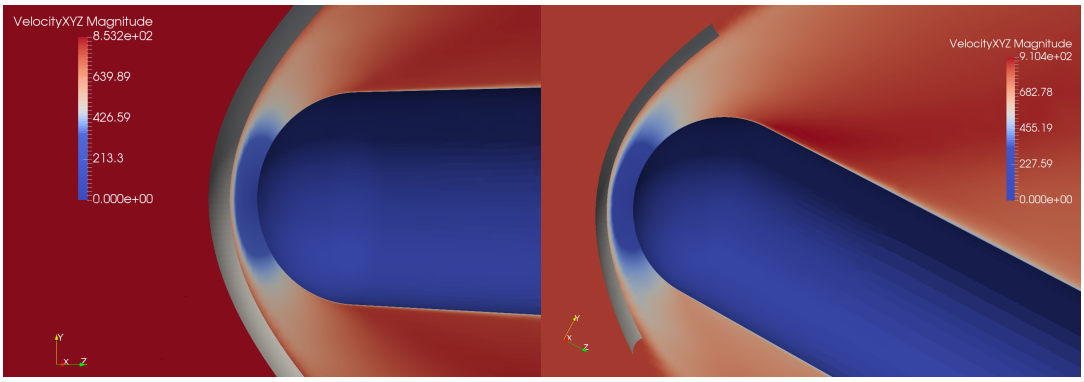

(a) α=0 ° (b) $\alpha = 20$ °

Figure 4.2.2: Representation of the fitted shock surface along with the flow solution for different cases of angle of attack.

The estimations of the errors made throughout the shock surface characterization are the following:

- a range of error of 0 and 1 [mm] in the shock coordinates detection,
- 1.8 [mm] of mean absolute error in the polynomial fitting of the obtained shock coordinates.

The fitting indeed shows non negligible errors with respect to the detected shock coordinates. Tightening the criterion of shock detection did not show noticeable improvements of the fitting nor of the shape of the fitted surface. Selecting a subset of shock nodes of interest allowed to slightly decrease the mean absolute error to 1.4 [mm].

Fitting of the shock surface with a non-uniform rational B-splines (NURBS) surface is an option that might produce better results. However the necessity of implementing the function in the `Zemax` function library imply a relatively high cost in development time. This option is therefore left for eventual further developments of the present approach.

4.3 Selection of GRIN$_{Air}$ nodes

The region of the flow that is perturbed by the proximity of the body and the resulting shock wave is now well determined since it is bounded upstream by the shock wave. The nodes of interest for computing the variation of index of refraction of the air are therefore located between the shock surface and the back of the optical window.

Two approaches are considered for the selection of these nodes of interest:

Shock bounded: The surface fitting the shock is used as an upstream boundary for the set of nodes; the other boundaries are defined such that they restrict the domain in accordance with the angles of view allowable by the optical window. In this case the boundary of the perturbed field is explicitly defined by the approximated shock surface.

Bounding box: The detection of the shock is used to formally determine the region in which the flow is perturbed. The nodes defining the air layer are selected such that they include the shock wave. Therefore the variations of flow quantities are represented by the interpolation conducted throughout the ray progression.

As stated in the previous section, the fitting errors of the shock surface are non-negligible. As a result, the representation of the orientation of the gradients at the interface might be flawed, introducing modelling errors in the optical model. The bounding-box, or "extended layer" approach is considered as an alternative to this issue. Since it only requires to include the shock and the perturbed flow, it might be applied easily to more complex flow configurations such as shock interactions. However the interpolation of the flow quantities through the shock might produce a damped representation of the gradients, with as a consequence a poor representation of the related optical effects.

Chapter 5

Modelling of the optical performances

The optical effects of the supersonic flow are modelled in `Zemax OpticStudio`, which implement a ray tracing method to model the light propagation in an optical system.

This modelling of the propagation of light is performed under a certain set of assumptions, under which the traditional Maxwell's equations are transformed into a simpler form. Indeed, in the case of the propagation of a light beam in an optical system, some effects linked to the wave nature of the light can largely be ignored, provided that the model is several order of size greater than the wavelength.

The purpose of the analysis is to determine the optical performances of the model, which are affected by aberrations generated by the considered aero-optical effects. Based on the working principle of the test case, a missile homing system, several configurations are considered in order to represent the rotation of the optical sensor behind the optical window. Different angles of sight are therefore considered, as well as two different wavelengths. The consistence of the results obtained is discussed in the light of the theoretical behavior of the light rays in a non homogeneous medium.

An evaluation of the modelling errors allows to estimate the precision achieved on the performances computed. Considering the multiple stages of modelling and processing involved in the whole work flow, the probable sources of errors are identified. Improvements of the methods used are suggested for future developments.

Finally the results are interpreted in the context of the missile guidance system, and an evaluation of the practical implications of the optical performances is proposed.

5.1 Theoretical background

The present theoretical background on optics aims to introduce the different concepts necessary to apprehend the phenomena that occur in the studied case. The developments are therefore sparse since they have no critical interest in the present case; emphasis is placed on the results and main expressions, the intermediary steps being available in the reference books cited throughout this section.

In classical electrodynamics, light is described as an electromagnetic wave. If the wavelength of the light is small in comparison to the size of the components, the approximation of geometric optic can be used. Conversely, if the characteristic dimension of the optics is close to the wavelength, the wave nature of light dominates.

5.1.1 Geometric optics approximation

The geometric optics approximation is a simplification of the general wave optics: phenomena related to the electromagnetic wave nature of the light, such as interference and diffraction, are neglected. This constitutes the "eikonal approximation" which states that the light propagates like rays, i.e. rectilinearly in an homogeneous medium. Such simplifications of the behavior of the light are made under the assumption that the dimensions of the optical elements and of the beam are several order of magnitude greater than the wavelength of the light.

The equations of geometric optics can be derived from Maxwell's equations; the present section only presents the results of the developments from the Springer handbook of optics ([Trä07]) and Hecht ([Hec02]). Considering an isotropic, linear and dielectric material, the electromagnetic equations writes:

$$\boldsymbol{\nabla} \times \boldsymbol{E}(\boldsymbol{r},t) = -\frac{\partial \boldsymbol{B}(\boldsymbol{r},t)}{\partial t}, \tag{5.1.1}$$

$$\boldsymbol{\nabla} \times \boldsymbol{H}(\boldsymbol{r},t) = \frac{\partial \boldsymbol{D}}{\partial t} + \boldsymbol{j}(\boldsymbol{r},t), \tag{5.1.2}$$

$$\boldsymbol{\nabla} \cdot \boldsymbol{B}(\boldsymbol{r},t) = 0, \tag{5.1.3}$$

$$\boldsymbol{\nabla} \cdot \boldsymbol{D}(\boldsymbol{r},t) = 0 \tag{5.1.4}$$

with the following physical quantities:

- $\boldsymbol{E}$ the electric field vector
- $\boldsymbol{H}$ the magnetic field vector,
- $\boldsymbol{D}$ the electric displacement field,
- $\boldsymbol{B}$ the magnetic induction field,
- $\boldsymbol{j}$ the electric current density.

These are functions of the position vector $r = (x, y, z)$ and of the time t.

Introducing the material equations linking these different electromagnetic quantities with each other:

$$\boldsymbol{D}(\boldsymbol{r},t) = \epsilon(\boldsymbol{r})\epsilon_0\boldsymbol{E}(\boldsymbol{r},t), \tag{5.1.5}$$

$$\boldsymbol{B}(\boldsymbol{r},t) = \mu(\boldsymbol{r},t)\mu_0\boldsymbol{H}(\boldsymbol{r},t), \tag{5.1.6}$$

$$\boldsymbol{j}(\boldsymbol{r},t) = \sigma(\boldsymbol{r})\boldsymbol{E}(\boldsymbol{r},t), \tag{5.1.7}$$

ϵ being the dielectric function, μ the magnetic permeability and σ the specific conductivity. ϵ_0 and μ_0 are respectively the dielectric constant and the permeability of the vacuum.

Researching solutions in the form of a monochromatic wave, the electric and magnetic fields are expressed as:

$$\boldsymbol{E}(\boldsymbol{r},t) = \boldsymbol{E_0}(\boldsymbol{r})e^{i(\phi(\boldsymbol{r})-\omega t)}, \tag{5.1.8}$$

$$\boldsymbol{B}(\boldsymbol{r},t) = \boldsymbol{B_0}(\boldsymbol{r})e^{i(\phi(\boldsymbol{r})-\omega t)}, \tag{5.1.9}$$

A separation in the time scales of the variations can be performed, considering that the envelope of $\boldsymbol{E_0}$ and $\boldsymbol{B_0}$ vary in several length scales greater than the wavelength, while the characteristic scale of variation of the phase ϕ is of the wavelength. Note that *omega* is the pulsation $[\mathrm{rad}\cdot\mathrm{s}^{-1}]$ This allows to consider that the wave behave locally as a plane wave, which components $\boldsymbol{E_0}$,$\boldsymbol{B_0}$ and $\boldsymbol{\nabla}\phi$ are orthogonal. Under these considerations, the time-independent Maxwell's equations can be developed. Considering the limiting case where $\lambda \to 0$, and defining an optical path $\boldsymbol{r}(s)$ parametrized by the curvilinear coordinate s, the combination of the Maxwell's equations yields, for a light ray:

$$\boldsymbol{\nabla}\phi(\boldsymbol{r}(s)) = n(\boldsymbol{r}(s))\frac{\omega}{c}\boldsymbol{u}(\boldsymbol{r}(s)), \tag{5.1.10}$$

Where $\boldsymbol{u}(\boldsymbol{r}(s)) = \dfrac{\mathrm{d}\phi(\boldsymbol{r}(s))}{\mathrm{d}s}$ is the unit vector of direction of propagation of the ray, $n(\boldsymbol{r}(s)) = \dfrac{v(\boldsymbol{r}(s))}{c}$ is the local index of refraction, with

- $v(\boldsymbol{r}(s))$ the local speed of light in the medium,
- c the speed of light in vacuum.

Derivation with respect to the curvilinear coordinate yields the *eikonal* equation:

$$\frac{\mathrm{d}(n\boldsymbol{u})}{\mathrm{d}s} = \boldsymbol{\nabla}\boldsymbol{n}, \tag{5.1.11}$$

which is the differential equation for a ray in a general inhomogeneous, isotropic and linear substance. Such materials presenting an index of refraction depending on the position (i.e. possessing an internal GRadient of INdex n) are often called graded index materials, or GRIN materials. The behavior of a light ray in such a medium can be deduced from the following interpretation of the eikonal equation: the direction of propagation of the light tends to align with the gradient of index of refraction. Conversely a light ray propagates in straight line in an homogeneous material.

5.1.2 Wave optics and diffraction

The wave nature of the light actually characterizes entirely its behavior; the real propagation of the light in a material is in fact diffusion, as well described by Hecht ([Hec02] Chapter 4). The approximation of propagation in rays neglects the lateral diffusion inherent to the progression of light in any medium.

As established previously, the effects related to the wave nature of light can largely be ignored under the geometric optic conditions. However the finite size of the elements of an actual optical system, in particular their apertures, introduces perturbations due to diffraction. Indeed, the system can only intercept a fraction of the incident wave of light, which will be partially diffracted and therefore modified. This means that there is always a deflection with respect to the rectilinear propagation of the rays.

The existence of a stigmatic optical system, i.e. a system which produces a perfect image of a point emitting rays, is made impossible by the presence of this diffraction effect: the quality of the optical system is said to be limited by diffraction. The practical measure of this limitation is defined as the spatial resolution of the system: in the imaging plane, it is the radius of the smallest spot to which the rays of a beam can be focused. It is obtained by the Rayleigh criterion, which writes ([Hec02]):

$$\Delta l = 1.22 \frac{f\lambda}{D}, \tag{5.1.12}$$

with

- f the focal length of the optical system,
- D the diameter of the light beam, which is equal to the diameter of the (circulat) aperture,
- λ the wavelength of light.

It is equal to the Airy radius, which defines the region within which most of the light intensity is focused in the Airy diffraction pattern, i.e. the central disc in Fig. 5.1.1. This Airy radius from Equ. 5.1.12 defines the diffraction limit of the optical system.

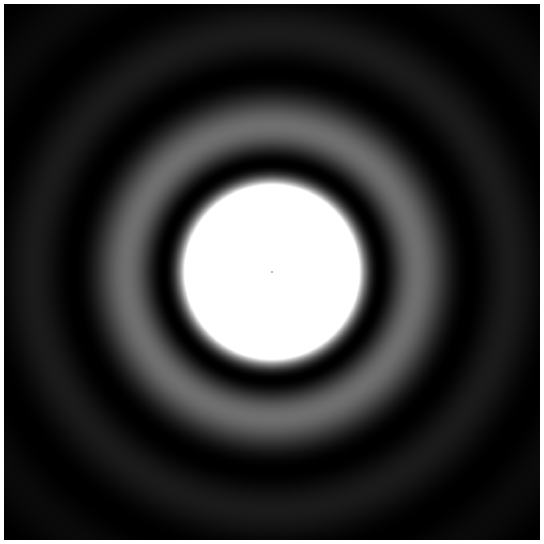

Figure 5.1.1: Fraunhofer diffraction of a circular aperture (Airy pattern).

5.1.3 Optical aberrations

In practice there is no such thing as a perfect optical system and elements; there are always aberrations that deteriorate its imaging quality. Optical aberrations can be conceptualized in terms of wave or rays aberrations. Fig. 5.1.2 illustrates the case of an aberrated converging beam. A real front wave is considered at the exit pupil of an optical system; the rays close to the optical axis are *paraxial* rays, which define the paraxial focus point P in the focal plane of the system. The real wave front can be compared to a perfect, spherical wave front of center P: away from the paraxial region, there are differences in the optical path followed by the rays of these two fronts. These are called wave aberrations or wave front errors, and are usually expressed in terms of a multiple of the wavelength (wave unit).

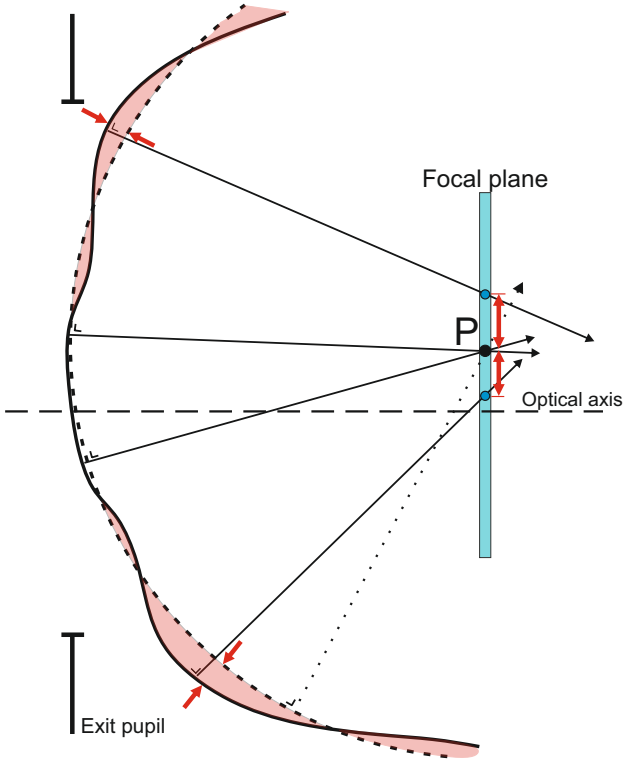

Figure 5.1.2: Representation of the wave and ray aberrations by comparison of the real wave front (solid curve) with an ideal, spherical wave front (dashed curve).

The rays with aberrations do not intersect the focal plane in P; instead they have lateral deviations Δx and Δy from P, which are called ray aberrations. These deviations can be displayed on what is called a spot diagram: the points of intersection of a beam of rays with the image plane are displayed, which is another indicator of the optical aberrations of the system.

5.1.4 Index of refraction

The index of refraction of a medium characterizes how light propagates through it. It is described as the ratio between the speed of light in vacuum and the speed of light in the considered medium: $n = \frac{c}{v}$. In isotropic media, the index of refraction depends on material, the temperature and the wavelength of the light.

The change of refractive index due to a change of temperature is called the thermo-optic effect. In the case of optical glasses, it can be described with the following formula, as developed by Schott ([Sch]) :

$$\frac{\mathrm{d}n_{abs}(\lambda, T)}{\mathrm{d}T} = \frac{n^2(\lambda, T_0) - 1}{2n(\lambda, T_0)} \Big(D_0 + 2D_1\Delta T + 3D_2\Delta T^2 + \frac{E_0 + 2E_1\Delta T}{\lambda^2 - \lambda_k^2} \Big), \tag{5.1.13}$$

where

- T_0 is the reference temperature (20 °C), T the temperature and ΔT the temperature variation,
- λ is the wavelength of the light considered in vacuum,
- D_0, D_1, D_2, E_0, E_1 and λ_k are constants depending on the glass type.

In the case of fluids, the refraction index can be directly related to the index of refraction of the fluid by the Gladstone-Dale relation ([HD64]):

$$\frac{n - 1}{\rho} = \mathcal{K}, \tag{5.1.14}$$

where

- ρ is the density of the medium,
- $\mathcal{K} = \mathcal{K}(\lambda)$ is the Gladstone-Dale constant for a given wavelength, with

$$\mathcal{K}(\lambda) = \big(2.192539 + \frac{0.01785076}{\lambda^2}\big) \times 10^{-4} \qquad \text{for air.} \tag{5.1.15}$$

Kharitonov ([KKS76]) suggests that the Gladstone-Dale constant remains practically unchanged for temperatures up to 6000 [K]; no dependence on the temperature is therefore considered for the G-D constant of the air. However the density, pressure and temperature of a gas are dependent thermodynamically; the refractive index itself therefore depends on the temperature conditions.

5.2 Approach for modelling the optical behavior

The approach to evaluate the optical aberrations consists in defining an optical system whose elements are defined such that they reproduce the optical properties of the different media and phenomena. The optical window can directly be seen as a lens, being a solid with well defined surfaces. The air layer can be conceptualized as a "pseudo lens" or a stratified assembly of GRIN layers.

The propagation of the light in the optical system is modelled under the geometric optic approximation, under which the aberrations linked to the wave nature of the light are disregarded. However the limit of diffraction of the system is evaluated in order to provide a scale of comparison for the ray aberrations generated by the system: if the aberrations are smaller than the limit of diffraction of the system, they can as well be neglected. This consideration does not concern the boresight, which is affected by the aberrations anyway.

The many parameters of the optical model such as the aperture, angle of sight and focal length are inspired or extrapolated from data available on the Stinger optical system. A dual infrared-ultraviolet sensor is considered, as it is embed on the last model of Stinger; the influence of the light wavelength on the aberrations can therefore be studied.

5.2.1 Definition of the optical model

A nominal model was created, including a dome figuring the optical window and a plane surface lens representing the air layer, with no optical properties defined yet and placed at an arbitrary distance.

At this point the configuration of the optical sensor should be considered. In Sec. 3.2.1, the optical sensor was not included in the physical model since it was assumed not to interact thermally with the structure (a hypercooling system is present in the actual sensor module). However it defines critical parameters of the optical model, such as the aperture or the considered angles of sight. As depicted in Fig. 5.2.1 and inspired from the actual geometry (see Fig. 5.2.1a) the optical device is mounted on a steerable turret inside the optical window. The technology of the sensor itself is unknown; a reasonable assumption is to consider it at the image plane, on which a lens focuses the incoming rays.

This lens defines the aperture of the model, which is fixed to 10 [mm] of diameter. It also defines the diameter of the considered light beam. The focusing lens is considered as a perfect optical element, which does not generate any optical aberration. Initially, a focal length of 20 [mm] is defined. A defocus is brought by the presence of the dome, which is mitigated by adjusting the focal length using the *Quickfocus* tool from `Zeemax`.

The resulting nominal optical model is displayed in Fig. 5.2.1b. Two angles of sight are considered, with a tilt of the optical device about the x axis of respectively 0 and 20°.

As described in technical description of the Stinger missile ([Joh12] and [Mil]) the latest developed versions are equipped with a dual infrared and ultraviolet sensor. This allows the missile to ignore most of the existing counter measures such as flares or IR jamming. The wavelengths considered are 4 [μm] for the IR and 0.25 [μm] for the UV, as these correspond respectively to the radiation from exhaust gas and radiation from the heated fuselage by the engines ([Mil]).

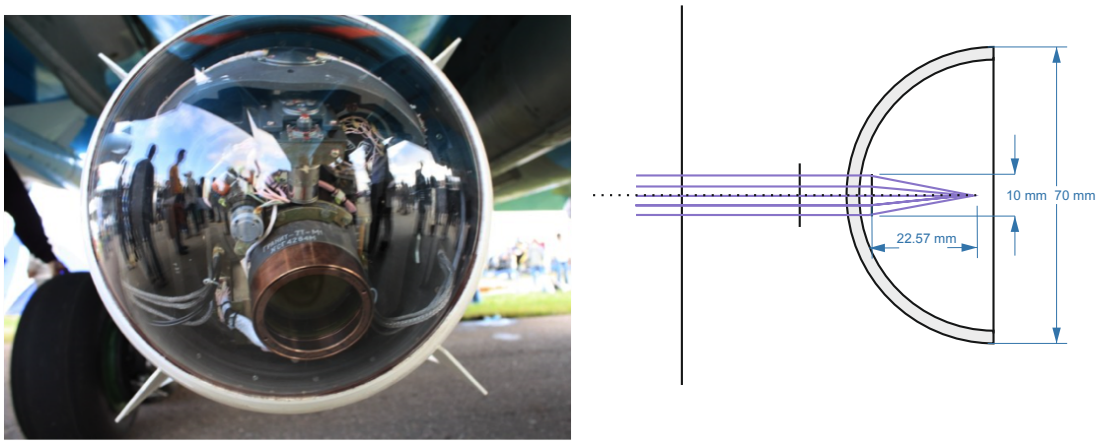

(a) Actual seeker of a FM-92 "Stinger" missile.

(b) Representation of the nominal optical model.

Figure 5.2.1

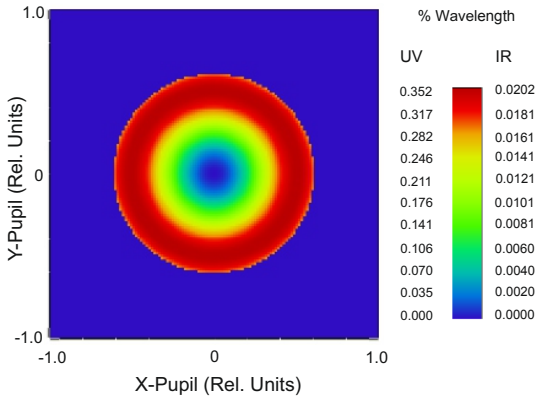

(a) Wavefront aberrations relative to the nominal model, expressed in fraction of the wavelength considered.

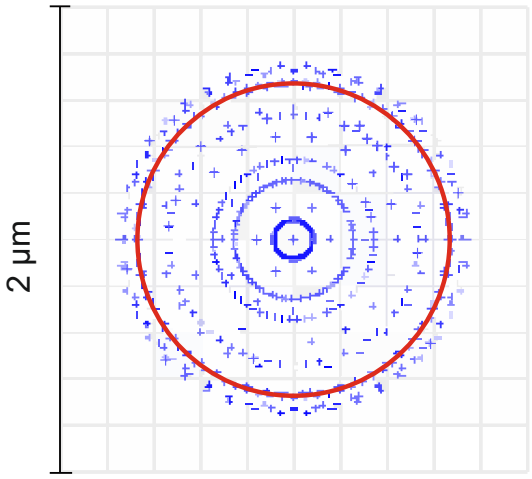

(b) Ray aberrations relative to the nominal system for a wavelength of 0.25 [μm]. The red circle figures the Airy disk relative to the UV radiation for the system.

Figure 5.2.2: Wavefront and ray aberrations relative to the nominal model.

The nominal model is still imperfect and presents optical aberrations due to the spherical dome. These aberrations are computed by ray tracing and displayed in Fig. 5.2.2. On Fig. 5.2.2b the nominal ray aberrations are displayed and can be compared to the limits of diffraction relative to the two considered wavelengths. The nominal aberrations are limited to a radius of 0.75 [μm]; this is smaller than the diffraction limit relative to the infrared, which equals 11.02 [μm] from Equ. 5.1.12. On the other hand the ray deviations are slightly greater than the Airy disk relative to the ultraviolet, which has a radius of 0.69 [μm]. This nominal geometrical blurring is almost negligible considering the amplitudes of the aberrations produced by the flow field and the dome.

This is visible on the wavefront aberration map (Fig. 5.2.2a), where the error grows up to 0.35 waves for the UV while it is less than 0.1 wave in the case of the infrared. Note that due to the absence of difference between the wave front map for the two wavelengths, these are presented as in Fig. 5.2.2a in the following: one map is represented with a double sided color scale for UV and IR.

In Sec. 4.3, two approaches were defined for selecting the set of nodes defining $GRIN_{air}$: a shock-limited set and a bounding-box limited set. In both cases the GRIN layer is defined from the file transmitted to `Zeemax`; in practice "dummy" surfaces (with no optical properties) are created in order to define the boundaries of the layer. In the case of the shock-limited approach, the coefficients of the polynomial fitting performed as detailed in Sec. 4.2.2 are transferred as well, and define the shock surface as the boundary of the GRIN layer. The resulting layout of the optical model in the case of the shock limited approach is shown in Fig. 5.2.3.

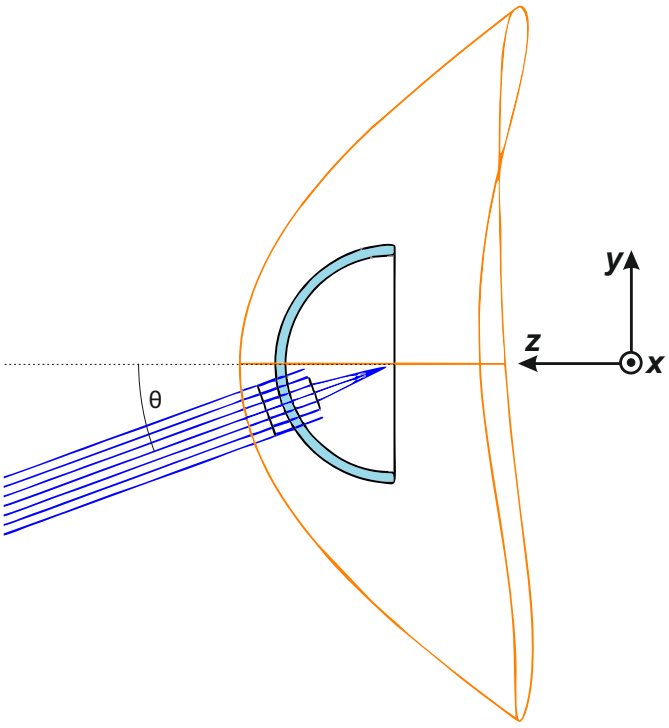

Figure 5.2.3: Representation of the optical model with the updated shock surface, in the case of an angle of attack $\alpha = 0$, and an angle of view of 20 °.

5.2.2 Ray tracing in GRINs

The propagation of rays in an optical system can be simulated by ray tracing. Its principle follows the eikonal equation; as stated previously, in an homogeneous isotropic material the ray propagates rectilinearly. At an interface with another material, the point of intersection of the ray with the surface is computed, and at this point the ray is refracted depending on the properties of the interface and of the other medium. If the second material is inhomogeneous, i.e. is a GRIN material, the trajectory of the ray is computed by solving Equ. 5.1.11 numerically; the ray path is curved. In practice the integration of the ray equation requires the definition of a spatial step. This parameter is indeed important for the optical modelling, and it must be assured that the time

step is appropriate, i.e. a further diminution of this parameter does not affect the solution.

The nodal values of the index of refraction of the air layer, defining $GRIN_{air}$, are obtained from the node set defined at the end of the intermediary processing, described in Sec. 4.3. As described in Sec. 5.1.4 the index of refraction is obtained from the density by using Equ. 5.1.14.

Similarly, the discrete value of the refractive index of the optical dome are obtained from the nodal values of temperature by using Equ. 5.1.13. The coefficients relative to the ALON are obtained from [Cha90]; note that only D_0 and D_1 are available. The value of the refractive index $n(\boldsymbol{r})$ at any point in the medium is obtained by interpolation of the values at the neighbouring nodes.

In the present application, the ray tracing is sequential: the user defines the order in which the different surfaces of the optical system are passed by a ray. This method present the advantage of being relatively cheap in terms of computational cost; however it cannot represent phenomena such a illumination in a system or stray light. In such case, the non-sequential ray tracing is used: there is no predefined sequence of interactions of the rays with the different surfaces. The interactions between rays and optical elements are determined solely by the position and properties of the objects, and by the trajectories of the rays. It is therefore able to perform stray light analysis. The non-sequential ray tracing method is very powerful, however the computational cost is relatively high. In the absence of a particular need for this method, the sequential ray tracing is used instead.

5.3 Aero-optical aberrations: analysis and discussion

The propagation of the rays in the optical system is performed in `Zemax`. In a first time the analysis of the optical aberrations is performed separately for the air layer and for the optical dome, in order to evaluate their respective contributions to the total aberrations generated.

For the air layer, the results obtained from the two approaches followed to define the GRIN material are compared. The optical aberrations produced by the model are discussed in terms of correspondence with the behavior of the rays as it can be expected from the theory.

Errors of modelling of the optical performances are ineluctably introduced by the approximation of the shock surface and by the interpolation of the index of refraction. As a consequence the results differ to some extent from what is expected theoretically. These resulting errors on the optical behavior of the system can be estimated and put in perspective with the wavelength of the light considered in the model.

Considering the probable sources of errors, different workarounds are proposed for further developments in order to achieve a better precision on the modelling of the optical performances.

5.3.1 Aberrations due to the air layer

The strong variations of density through the shock and the isentropic compression near the stagnation point in the subsonic region of the flow introduce gradients of index of refraction in the air layer. According to the eikonal equation, these gradients produce optical aberrations, that are studied in terms of ray deviations and wavefront aberrations. The interpretation of the ray equation predicts that the variations of a ray trajectory are aligned with the local refractive index gradient, and as such with the density gradients. Therefore the visualisation of iso-density lines can provide an insight on how the ray might be deflected. Fig. 5.3.1 depicts expected rays deviations in the case of an angle of attack of the body with the flow of 0°. If an angle of view of 0°is considered, the rays are expected to undergo a focusing effect by the air layer, which translates by a defocus on the focal plane. On the other hand for other angles of view a boresight deviation is expected, depending on the angle of the incident ray with the normal at the shock. Note that a ray parallel to the z axis and passing exactly by the center of the shock should not be deflected.

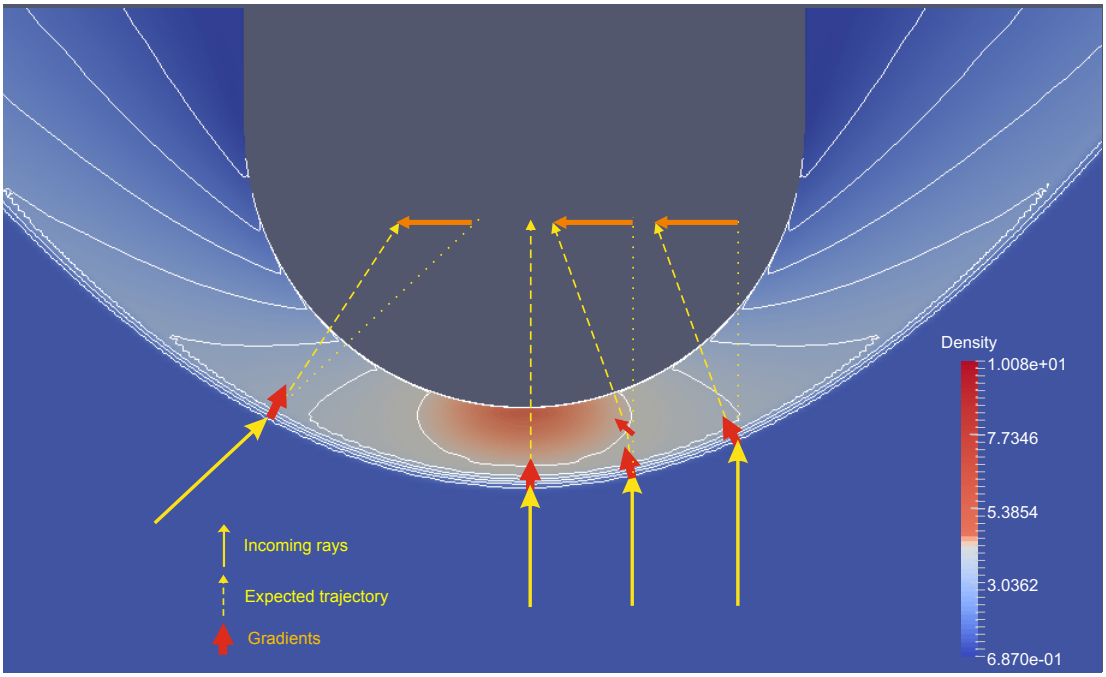

Figure 5.3.1: Representation of the expected ray deviations, using a visualization of isovalues of density of the flow.

Two series of optical simulations are conducted, varying by the method of representation for the GRIN layer: whether the shock-limited or bounding-box-limited (cf Sec. 4.3). The comparison of the results between the two approaches is used as a basis to discuss the consistency of the modelled optical performances. The optical aberrations produced by the flow effects should be consistent for the different flow configurations and angles of view considered. A lack of regularity in the results obtained, a marked or systematic mismatch with the theoretical expectations might indicate that the approach is not suitable or generates too many errors with the present conditions.

The ray aberrations produced by the air layer in the flow configuration corresponding to a 0°angle of attack are presented in the set of spot diagrams in Fig. 5.3.2. As expected, a defocus is induced by the gradients in the air layer: the different radii of dispersion included in Tab. 5.3.1 are several times higher than the radius of the nominal aberrations (which was equal to 0.75 [μm], Fig. 5.2.2b). In the case of the UV radiation the spot diagram exceeds by far the limit of diffraction of the system (0.69 [μm]); on the other hand the ray aberrations related to the infrared are still below the Airy radius of the system for infrared (11.02 [μm]).

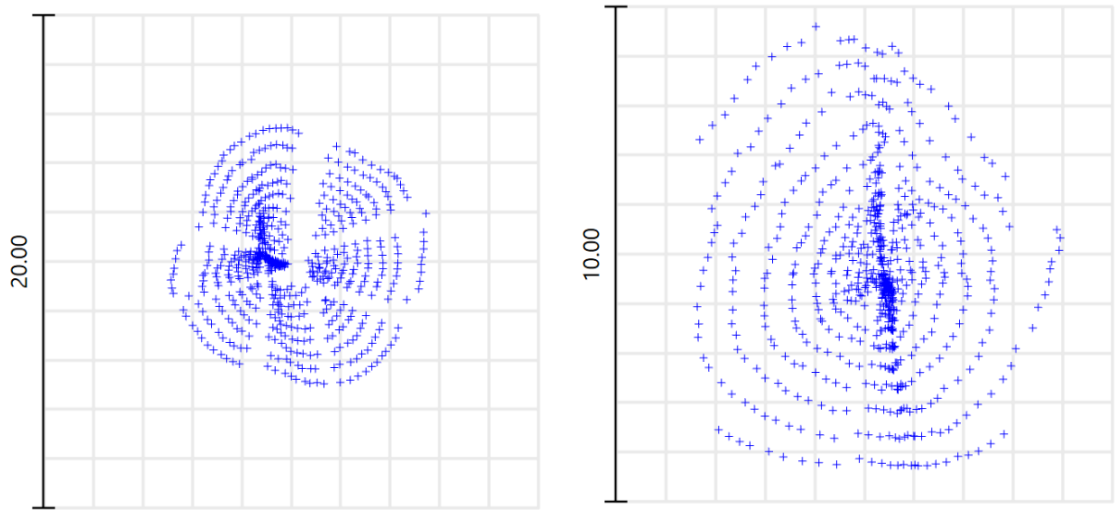

(a) Extended layer, $\theta = 0$ °.

(b) Extended layer, $\theta = 20$ °.

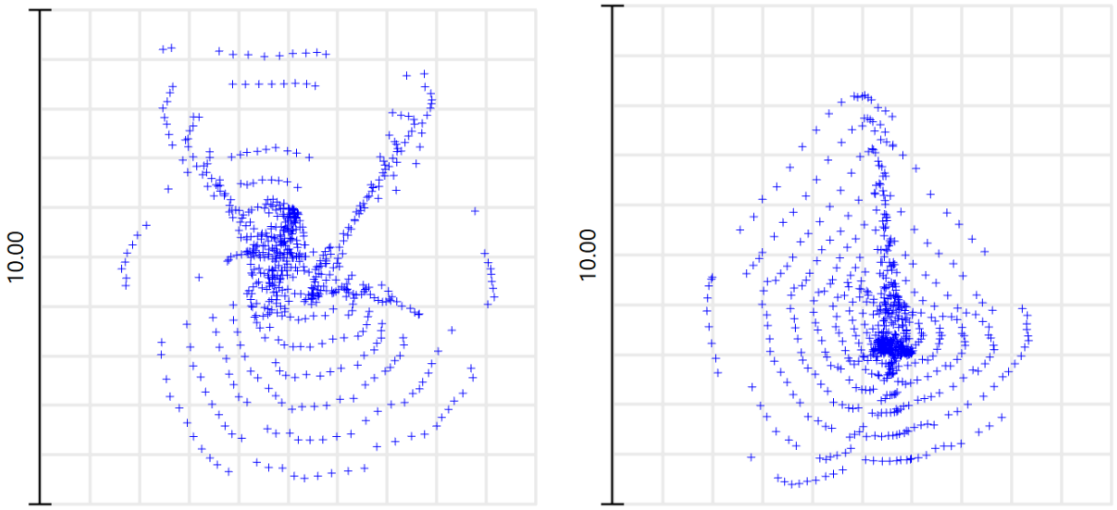

(c) With shock surface, $\theta = 0$ °.

(d) With shock surface, $\theta = 20$ °.

Figure 5.3.2: Comparison of the ray aberrations on spot diagrams between the two methods of GRIN definition, with a flow case corresponding to $\alpha = 0°$, and for a wavelength $\lambda = 0.25$. Note that the grid scale is in [μm]

As a matter of fact the dispersion patterns of the spots are dissimilar between the two methods, particularly for the angle of view of 0°: with the shock surface considered, an important proportion of the spots are limited to a radius of 1 [μm], which is consistent with the expectations that the rays should not be slightly deflected near the normal part of the shock. However the dispersion pattern is asymmetric, which should no be the case; this is due to the shock surface which inevitably suffers from fitting errors. On the other hand the extended layer provides a symmetric result, with

a greater defocus. In terms of spots dispersion the results are much more similar for the case of an angle of sight of 20°: as seen on Fig. 5.3.2d and 5.3.2b the spot diagrams both present a cluster of weakly scattered spots surrounded by the traces of the rays located on the outside of the beam, which are more dispersed.

	Extended layer			Shock-limited		
θ	radius [μm]	x offset [μm]	y offset [μm]	radius [μm]	x [μm] offset	y offset [μm]
0	5.08	-0.09	0.08	4.3	-0.19	-0.08
20	4.09	0.16	0.3	4.2	0.3	-1.18
0	5.8	-0.11	0.09	4.89	0.25	-0.09
20	4.7	0.18	-0.3	4.81	0.39	-1.3

Table 5.3.1: Ray aberrations relative to the GRIN layer, obtained respectively by the Extended layer and Shock-limited methods for the two wavelengths considered: $\lambda = 4$ [μm] (in red) and $\lambda = 0.25$ [μm] (in blue). The angle of sight is denoted θ above.

The two approaches for the GRIN definition can be further compared in terms of x and y offset of the centroïd of the spots. This parameter is of the most importance in the context of the studied case (a missile guidance system): it defines the boresight error of the optical system, i.e. the deviation between where the image is "seen" and where the object actually is. As shown in Tab. 5.3.1, the x offsets computed are in the order of $\sim 10^{-1}$ [μm] for angles of view of 0 and 20 °. Considering the symmetry of the model, flow solution and (theoretically) of the shock wave, the boresight deviation in this direction should be equal to zero. This mismatch with the theory is probably due to the level of approximation used in the optical model: as it was foreseen in Sec. 4.3 the interpolation of n and the fitted shock surface introduce errors on the orientation of the gradients. It can be noted that the y offsets for the angle of sight of 0°also scale as $\sim 10^{-1}$ [μm] whereas the theory forecasts a zero value. It therefore appears clear that an error on boresight of the order of $\sim 10^{-1}$ is present in the modelling. It can be noted that in the case where the fitted shock surface is employed the x offsets are even larger.

An important difference between the two approaches appears for the y offset at 20°of view angle: with the extended layer the overall deviation of the beam is very small, contrary to what is expected from theory. Indeed, as shown in Fig. 5.3.1 an incoming ray presenting an angle of sight greater than 0 should be affected by a ray aberration, in the present case a deflection downwards. Consistent results are obtained with the model where the surface is defined, with y offsets of respectively -1.18 and -1.3 [μm] for IR and UV.

This "tilt" of the beam of rays at θ =20°is observable on the wave front aberration map in Fig. 5.3.3: the wavefront function shows a vertical gradient distinctive of a tilt of the rays. This effect can be removed from the map by `Zeemax` as shown in Fig. 5.3.3b, in the hope of further analysing the wavefront aberrations. The usual methodology is to perform a fitting of the wavefront aberration function with Zernike polynomials: these are of the same form as the types of aberrations observed in practice, and can therefore be used to express any wavefront perturbation in terms of familiar optical effect. In the present case, the Zernike decomposition presents high fitting errors

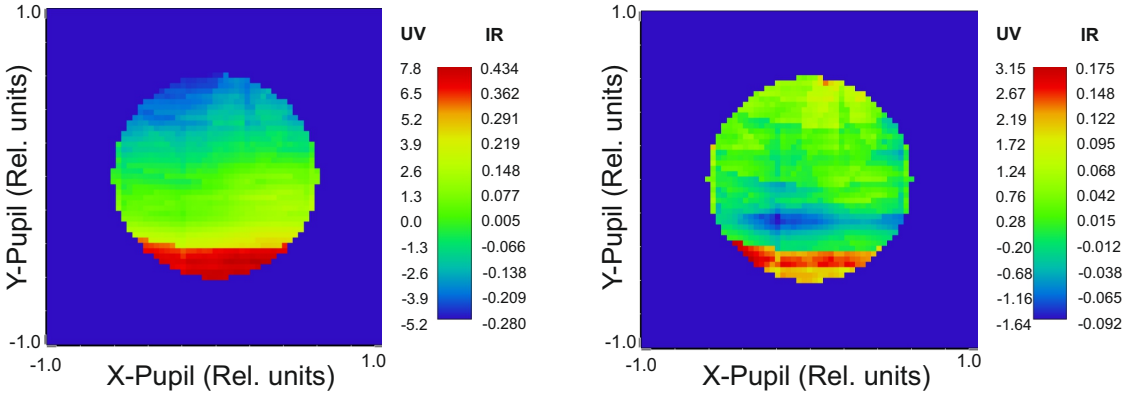

(a) Normal case (no tilt removal).

(b) Remaining wave aberrations after tilt removal.

Figure 5.3.3: Wavefront aberrations in the case of a 20°angle of sight, $\alpha = 0$.

and is not reliable.

The results obtained for the other flow configurations are similar to the case of $\alpha = 0$:

– the extended layer approach produces large spot diagrams with very low offsets, even in angle of sight configurations where the theory predicts a deflection of the whole beam. This indicates that the shock wave is poorly depicted by the pure interpolation approach: the discontinuities of the shock are probably partially damped.

– The shock-limited approach provides consistent results for the other flow configurations: an offset of the rays is indeed observed for the angles of view that are not aligned with the normal of the shock surface. More specifically, in the flow configuration where $\alpha = 20°$, the rays aberrations relative to an angle of sight of 0°show a y offset of 1.7 [μm]. This is agreeing with the interpretation made of the ray equation, which indeed predicts a positive offset. The good concordance of the results with the theory is also observed for the flow case where the Mach number equals 4 and $\alpha = 0°$: the deflection of the rays along y increases to -2 [μm]. This is in accordance with the expected effect of the strengthening of the shock with the Mach number: the gradient of refractive index increases as well and the aberrations are amplified.

In the optical system where the shock surface is defined explicitly as the boundary of the GRIN layer, the optical performances are consistent with the perturbations expected in theory. The incident light beam is indeed affected by a defocus and a tilt about x, as it was forecasted. The solutions relative to this approach are therefore preferred for the following analyses. However the fitting errors of the actual shock and the ensuing errors of orientation of the normal to the surface result in modelling errors of the optical performances. In terms of boresight these errors of evaluation are comprised between 0.1 and 0.4 [μm]. The results from the optical modelling of the flow over the dome show that the flow-related disturbances in resolution are very weak for an operating wavelength of 4 [μm]: these are smaller than diffraction limited spot size represented by the Airy disk. Concerning the wavelength of 0.25 [μm], the nominal system already produced a focus shift increasing the geometrical blurring to a level slightly higher than the diffraction limit (though it might be considered negligible, see Fig. 5.2.2b). The flow produces an additional defocus that is several times larger than the Airy disk for this wavelength: the blurring effects of the air layer dominate the resolution in the case of the UV. In terms of boresight, the deviations introduced by the aero-optic effects are equal to respectively 0.052 and 0.057 [mrad]. The spurious

offsets along x are due to the fitting errors on the surface; they represent an error on the modelled boresight of $\approx 25\%$ (0.013 [mrad]).

In the light of the identified sources of modelling errors, several options can be suggested in the scope of improving the quality of the optic performances modelling:

- Further refine the interpolation mesh in the region of interest in order to improve the characterization of the shock surface and of the gradients.
- Perform a fitting of the shock nodes with a function defined locally, such as a NURBS surface. This would allow a better characterization of the normal to the surface, and therefore of the optical disturbances produced.
- Reduce drastically the spatial step of the ray equation integration. With a finer spatial discretization of the ray propagation, the gradients might be less damped in the shock wave region. However the computational cost of a small step everywhere is very high; a workaround might be to implement a high gradient detection criterion, which would trigger a local reduction of the step.

5.3.2 Aberrations due to the optical dome & combined effects

In a first time, the optical performances of the heated dome are modelled separately. The combined effects of the air layer and optical window are then considered, and the resulting optical performances can be discussed in terms of the relative importance of the contributions.

As it was established in Sec. 3.4 the temperature of the optical dome increases particularly in the vicinity of the stagnation point of the flow. Therefore there is a global increase of the index of refraction of the dome material as well as a gradient of index of refraction due to the non uniformity of the temperature of the dome. The relative refractive index of the optical window is shown in Fig. 5.3.4: it is defined as the ratio of the local n with the index of refraction of the window at a reference temperature. It appears clearly that there is a great increase of the refractive index of the whole dome, whereas the variations of this index over the optical window are weak. Indeed due to the relatively high thermal conductivity of the material (13 [$\mathrm{Wm^{-1} \cdot K^{-1}}$], $\sim$ 13 times higher than Pyrex or ordinary glass) there are no spectacular gradients of temperature in the dome.

The increase of temperature of the dome generates thermo-mechanical deformations: the external ("front") and internal ("back") faces of the dome are deformed. These deformations are non uniform and differ for the two surfaces, as shown in Fig. 5.3.5 for the flow case of $\alpha = 0$. Note that the difference of elastic deformation between the front and back surface increases off the center of the dome.

These effects combined alter the optical performances of the dome: a focus shift, as well as an important deviation of optical rays along y in the case of an angle of view of 20°, are observed. It can be noted that the ray deviation in x, which should theoretically be equal to 0, is of the order of $\sim 10^{-1}$ [μm]. This is consistent with the observation made previously that the errors performed in the modelling translates as $\sim 10^{-1}$ [μm] errors of the obtained boresight deviation.

The modelling of the optical performances shows that for a 0°angle of sight, the geometrical blurring produced is under the diffraction limited spot size for the infrared; on the contrary the dome-induced blurring dominates the resolution for the ultraviolet light, as shown in Fig. 5.3.6.

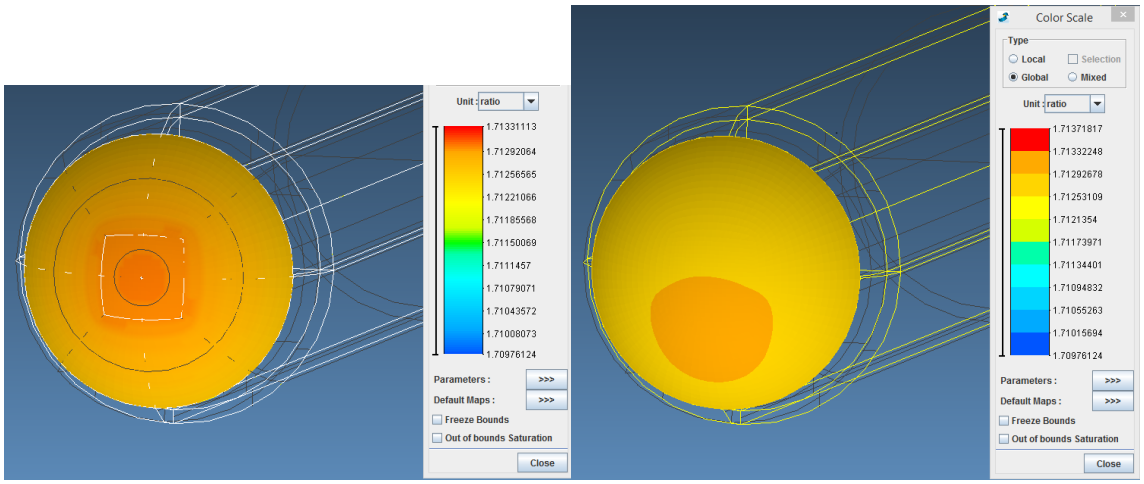

(a) Angle of view of 0°. (b) Angle of view of 20°.

Figure 5.3.4: Relative refractive index of the optical window.

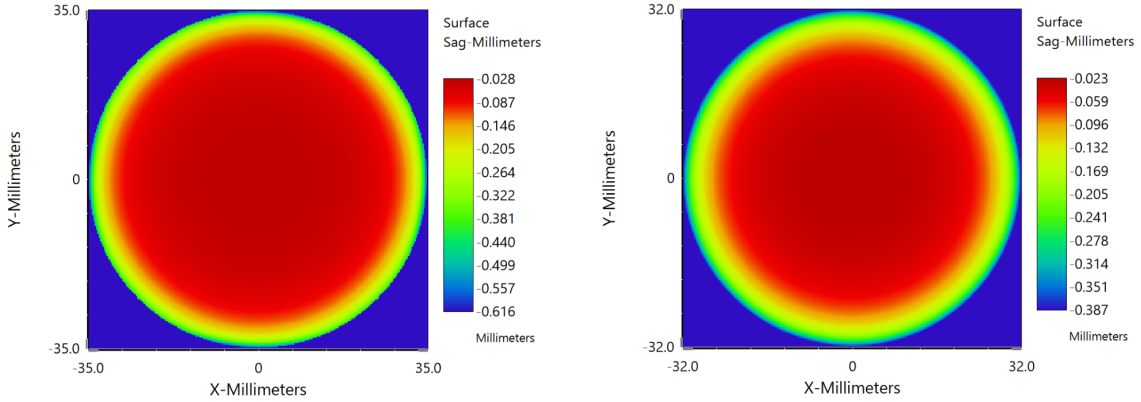

(a) Front face. (b) Back face.

Figure 5.3.5: Surface deviations due to elastic deformation for the front and back faces of the optical dome, in the flow case where $\alpha = 0$.

The focus shift at an angle of view of 20 °is significantly larger, and the geometrical blurring is increased to a level higher than the diffraction limit for both wavelengths.

The overall optical performances for the flow case where $\alpha = 0$ is depicted by the spot diagrams in Fig. 5.3.7. The ray deviation for the angle of sight of 20°equals 12.9 [μm], which is well equal to the sum of the contributions of the dome and the flow field. The boresight deviation is therefore equal to 0.57 [mrad]. For the other flow cases, it appears clearly that the effects of the dome are strongly coupled to the flow conditions:

- in the case of $M = 4$, $\alpha = 0$ the increased flow-field effects are largely exceeded by the rise in temperature of the window. The geometric blur is increased up to 43 [μm] with a boresight shift of 1 [mrad] for an angle of view of 20°.
- For an angle of attack $\alpha = 20°$, the asymmetric thermo-mechanical deformations produce a strong focus shift and rays deviations for all angles of view.

angle of view	GEO radius [μm]	x offset [μm]	y offset [μm]
0	6.12	-0.11	0.08
20	18.14	-0.103	-11.7

Table 5.3.2: Ray aberrations relative to the optical window for a flow configuration such that $\alpha = 0°$, and a wavelength $\lambda = 4$ [μm]. Scale of the diagram in waves ($\lambda = 4$ [μ]).

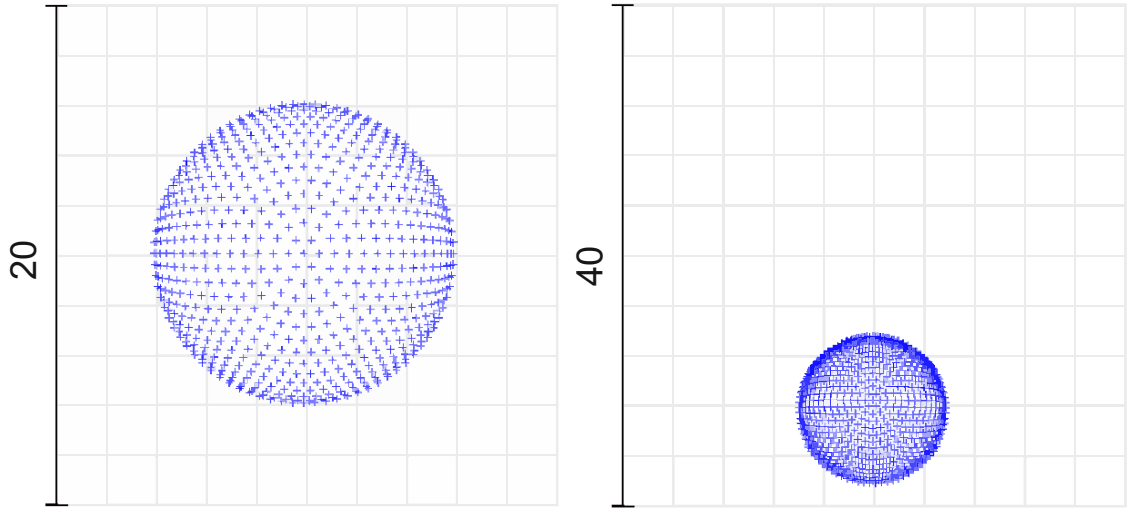

(a) Angle of view of 0°. GEO radius = 6.1 [μm] (b) Angle of view of 20°. GEO radius = 18.1 [μm]

Figure 5.3.6: Spot diagram representing the ray deflection and geometrical blurring for the different angle of view, in a flow configuration with $\alpha = 0$. Scale of the diagram in waves ($\lambda = 4$ [μ]).

The comparison of the respective effects of the flow and of the optical dome shows that the deformation and variation of index of refraction of the window strongly determines the optical performances: for $\alpha = 0$, $\theta = 0$, there is a ratio of 10 to 1 between the boresight deviation due to the dome, 0.51 [mrad], and due to the air layer, 0.052 [mrad]. As for all the flow and view angle configurations, both resolution and boresight are dominated by the effects of the dome. This is consistent with the observations of Tropf in [Tro+87], which clearly shown that the window has a significantly larger effect on optical performance. Note that the boresight deviation obtained is in the same order of magnitude as the boresight obtained by Tropf et al. in their optical simulations: a value of 0.5 [mrad] was computed. Due to the difference of flow case and the absence of information on the material used in their model, this matching of the results only validates the order of magnitude of the optical aberrations modelled in this work.

The UV are again very affected by the focus shift:for $\alpha = 0$, $\theta = 0°$and $\theta = 20°$the spot sizes are respectively $\sim$7 and $\sim$23 times larger than the diffraction limit of the system for this wavelength. The infrared are less affected: for an angle of view of 0°the perturbations in focus are smaller than the diffraction limit; for 20°it is only slightly above. The reason why most guidance system use infrared therefore appears clearly; the dual sensor in ultraviolet most probably provides assistance against counter-measures or background infrared radiation.

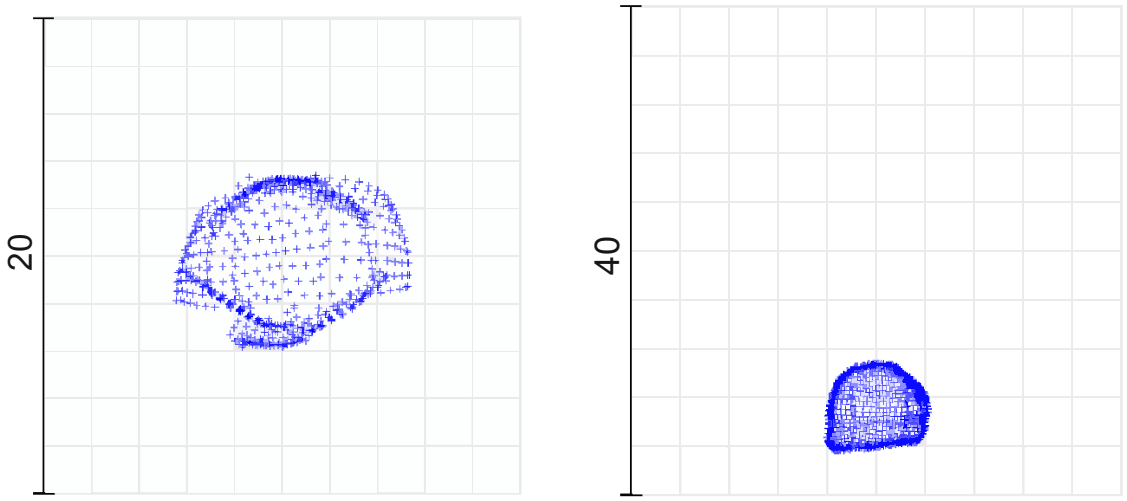

(a) Angle of view of 0°. GEO radius = 5.4 [μm] (b) Angle of view of 20°. GEO radius = 16.6 [μm]

Figure 5.3.7: Spot diagram representing the ray deflection and geometrical blurring of the combined effects of the dome and flow field, in a flow configuration such that $\alpha = 0$. Scale of the diagram in waves ($\lambda = 4$ [μ]).

5.3.3 Interpretation in the context of a guidance system

The optical performances of the system are expressed in terms of resolution and boresight. The degradation of these performances by the aero-optic effects leads to respectively a blurring of the image perceived and to a boresight error. These aberrations can be interpreted in the context of a missile guidance system: these can indeed be related to practical considerations for target acquisition and missile guidance.

The exact effect of blurring is difficult to interpret without precise technical data on the sensor and its operating principle. Qualitatively, the diminution of the resolution affects the target acquisition: beyond some point the image of the target is so blurred that it is no longer recognised as such.

The aiming error introduced by the aero-optic effects is directly obtained from the boresight shift. The angle deviation β is computed as

$$\tan(\beta) = \frac{\Delta b}{f}, \tag{5.3.1}$$

with Δb the boresight shift and f the focal length. Considering the configuration of $\alpha = 0$ and an angle of sight of 20°, Equ. 5.3.1 yields $\beta = 0.571$ [mrad].

A case study of a missile and its target, depicted in Fig. 5.3.8, allows to better visualize the degradation of the optical performances and its practical implications. The distance between the target and its virtual image is obtained by multiplying the distance target-sensor by the angle deviation, considering that $\tan(\beta) \approx \beta$. At a distance of 1000 [m] the target apparent position is shifted by 0.57 [m] from its actual position.

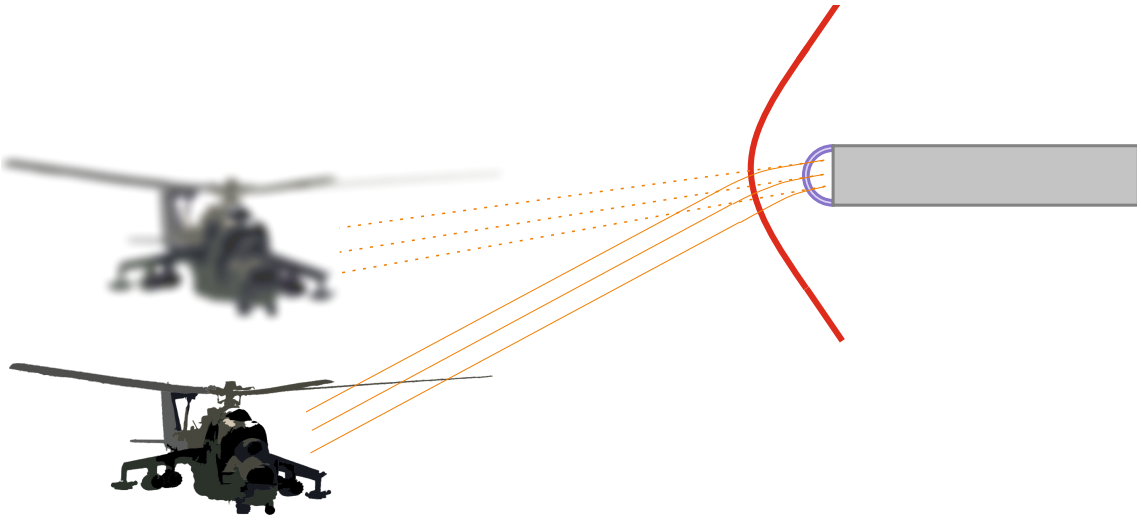

Figure 5.3.8: Representation of the degradation of the optical performances in the case study of a missile guidance system.

Chapter 6

Conclusion

With the aim of modelling aero-optic effects of a high speed flow, it was established that the presence of a shock wave simplifies the problem as the region of perturbed flow is clearly defined by the shock surface.

A model of a supersonic body equipped with an optical sensor was defined, based on the geometry of a famous infrared guided missile, the FIM-92 Stinger.

The combined presence of fluid, thermal and thermo-elastic phenomena required a fluid structure interaction simulation in order to provide consistent results. The flow, temperature and deformation fields indeed shown good concordance with what was expected from theory.

A processing of the fluid solution was developed, in which a detection method of the shock wave was successfully implemented. A parameter fitting of the shock was performed, with as a result a polynomial expression for the shock surface. Two different approaches of defining the GRIN layer were defined: the first by bounding the domain with the shock; the second by considering an extended layer of unperturbed flow beyond the shock.

Although promising, the second approach did not produced consistent results during the optical modelling, and was dismissed. The computation of the optical performances of the model by ray tracing shown that the aero-optic effects produced by the flow field are weak compared to the effects of the optical dome. In a typical configuration (angle of attack of $0°$, angle of view of $20°$), the disturbances in boresight shift were equal to 0.57 [mrad]. The geometrical blurring was found to strongly affect the ultraviolet wavelength. On the other hand, the infrared radiations were shown to be less affected by the focus shift.

Modelling errors produced notably by the imperfect fitting of the shock surface were detected, and estimated to scale as approximately 0.013 [mrad]. Fitting the shock with a NURBS surface is suggested for further development, in the scope of mitigating the errors introduced in input of the modelling. The extended layer approach might produce good results if coupled with a local decrease of the spatial step size through discontinuities.

Considering the leading role of the dome in the aero-optic disturbances, further studies could investigate the influence of the shape of the window or the material used on the optical performances. Modelling dome cooling methods in order to assess their efficiency on the reduction of optical aberrations could also be considered.

Bibliography

Articles

[KKS76] A. I. Kharitonov, K. S. Khoroshko, and V. P. Shkadova. "Temperature dependence of air refraction at high temperatures". In: *Fluid Dynamics* 9 (1976), pp. 851–853. DOI: 10.1007/BF01017444.

[Sva87] Krister Svanberg. "The method of moving asymptotes - A new method for structural optimization". In: *International Journal for Numerical Methods in Engineering* (1987), pp. 359–373.

[Tro+87] William J. Tropf et al. "Performance of optical sensors in hypersonic flight". In: *Johns Hopkins Technical Digest* 8.4 (1987).

[Cha90] Donald Dean Duncan Charles H. Lange. "Temperature coefficient of refractive index for candidate optical windows". In: *Proc.SPIE* 1326 (1990), pp. 1326-1326-8. DOI: 10.1117/12.22483. URL: https://doi.org/10.1117/12.22483.

[KS13] Masashi Kanamori and Kojiro Suzuki. "Three-Dimensional Shock Wave Detection Based on the Theory of Characteristics". In: *AIAA Journal* 51.9 (2013), pp. 2126–2132.

[S G15] M. R. Rennie S. Gordeyev. "Aero-optical measurements of High Mach supersonic boundary layers". In: *46th AIAA Plasmadynamics and Lasers Conference* (2015).

[Ant17] Jameson Antony. "Origins and Further Development of the Jameson–Schmidt–Turkel Scheme". In: *AIAA Journal* 55.5 (2017), pp. 1487–1510. DOI: 10.2514/1.J055493.

[FS17] N. Faujdar and S. Saraswat. "The detailed experimental analysis of bucket sort". In: (Jan. 2017), pp. 1–6. DOI: 10.1109/CONFLUENCE.2017.7943114.

[JB] Mori Mani John Ladd and W Bower. "Validation of Aerodynamic and Optical Computations for the Unsteady Flow Field About a Hemisphere-on-Cylinder Turret". In: *27th AIAA Applied Aerodynamics Conference. San Antonio, Texas.* ().

[ZE] Ilya A. Zilberter and Jack R. Edwards. "LES/RANS Modeling of Aero-Optical Effects in a Supersonic Cavity Flow". In: *47th AIAA Plasmadynamics and Lasers Conference, AIAA AVIATION Forum, (AIAA 2016-3531)* (). DOI: 10.2514/6.2016-3531.

Books

[HD64] J. H. and Dale. *Researches on the refraction, dispersion and sensitiveness of liquids*. Phil. Trans. Royal Soc. London, 1864.

[And01] John D. Anderson. *Fundamentals of aerodynamics*. fifth edition. McGraw-Hill., 2001.

[Ces01] Charles Massonet Serge Cescotto. *Mécanique des matériaux*. De Boeck & Larcier, 2001. ISBN: 2-8041-2021-X.

[Hec02] Eugene Hecht. *Optics, fourth edition*. Addison-Wesley, 2002. ISBN: 9780805385663.

[Str06] Gilbert Strang. *Linear algebra and its applications*. Belmont, CA: Thomson, Brooks/Cole, 2006. ISBN: 0030105676 9780030105678 0534422004 9780534422004. URL: http://www.amazon.com/Linear-Algebra-Its-Applications-Edition/dp/0030105676.

[Trä07] F. Träger. *Springer Handbook of Lasers and Optics*. Springer Handbook of Lasers and Optics. Springer New York, 2007. ISBN: 9780387304205. URL: https://books.google.be/books?id=YOHJGz-9UNoC.

[Fra12] David P. Dewitt Frank P. Incropera. *Foundation of Heat Transfert*. John Wiley & Sons, 2012. ISBN: 9780470646168.

[Joh12] Richard Chait John Lyons Duncan Long. *Critical Technology Events in the Development of the Stinger and Javelin Missile Systems: Project Hindsight Revisited*. 2012.

Online resources

[AD] Aubert and Duval. *X17U4 data sheet*. URL: https://www.aubertduval.com/alloy/766/. (accessed: 22/5/2018).

[Mil] MilitaryFactory. URL: https://www.militaryfactory.com/smallarms/detail.asp?smallarms_id=30. (accessed 3/06/2018).

[Sch] Schott. *TIE-19: Temperature coefficient of Refractive Index - July 2016*. URL: https://www.us.schott.com/advanced_optics/english/knowledge-center/technical-articles-and-tools/tie.html. (accessed:2/06/2018).

[Sur] Surmet. *ALON datasheet*. URL: www.surmet.com/docs/Product_sheet_ALON.pdf. (accessed: 22/05/2018).

Appendix A

FSI interactions

A.1 The Spalart-Allmaras turbulence model

The Spalart-Allmaras turbulence model is characterized by its robustness and ability to to treat complex flows.

It can be written in the following non-conservative form:

$$\underbrace{\Big(\frac{\partial}{\partial t}+\mathbf{v}\cdot\nabla\Big)\tilde{\mathbf{v}}}_{\text{advection term}}=\underbrace{\frac{1}{\sigma}\nabla\cdot\Big((\mathbf{v}+(1+c_{b2})\tilde{\mathbf{v}})\nabla\tilde{\mathbf{v}}\Big)}_{\text{diffusion term}}-\underbrace{\frac{c_{b2}}{\sigma}\tilde{\mathbf{v}}\Delta\tilde{\mathbf{v}}}_{\text{anti-diffusion}}+\underbrace{c_{b1}(1-f_{t2})\tilde{\mathbf{S}}\tilde{\mathbf{v}}}_{\text{production term}}-\underbrace{\Big(c_{w1}f_w-\frac{c_{b1}}{\kappa^2}f_{t2}\Big)\big(\frac{\tilde{\mathbf{v}}}{d}\big)^2}_{\text{destruction term}}+\underbrace{f_{t1}\Delta U^2}_{\text{trip term}} \tag{A.1.1}$$

with:

The production term is defined by the following functions:

$$\begin{aligned}
\chi &= \frac{\tilde{\mathbf{v}}}{\mathbf{v}},\\
f_{v1} &= \frac{\chi^3}{\chi^3+c_{v1}^3},\\
f_{v2} &= \Big(1+\frac{\chi}{c_{v2}}\Big)^{-3},\\
f_{v3} &= \frac{(1+\chi f_{v1})(1-\chi f_{v2})}{\chi},\\
\mathbf{S} &= |\nabla\times\tilde{\mathbf{v}}|,\\
\tilde{\mathbf{S}} &= \mathbf{S}f_{v3}+\frac{\tilde{\mathbf{v}}}{\kappa^2 d^2}f_{v2}.
\end{aligned} \tag{A.1.2}$$

where d is the distance to nearest wall. Note that χ is replaced by $max(\chi, 0.001)$ in the definition of f_{v3}.

The destruction term is constructed using the following functions:

$$
\begin{aligned}
r &= \frac{\tilde{\mathbf{v}}}{\tilde{\mathbf{S}}\kappa^2 d^2}, \\
g &= r + c_{w2}(r^6 - r), \\
f_w &= g\Big(\frac{1 + c_{w3}^6}{g^6 + c_{w3}^6}\Big),
\end{aligned}
\tag{A.1.3}
$$

Note that r is replaced by $min(r, 2)$ in order to prevent overflow.

In the production and destruction terms the function f_{t2} is defined such that:

$$f_{t2} = c_{t3} \exp\left(-c_{t4}\chi^4\right) \tag{A.1.4}$$

The trip term is defined using the following function:

$$f_{t1} = c_{t1} g_t \exp\Big(- c_{t2} \frac{\mathbf{S_t}}{\Delta U^2}(d^2 + g_t^2 + d_t^2)\Big) \tag{A.1.5}$$

where d_t is the distance to the nearest trip point, $\mathbf{S_t}$ is the vorticity at the wall at the trip point, and ΔU is the norm of the difference of velocity between the trip point and the field point where the trip term is calculated. The term g_t is defined by: $g_t = min\Big(0.1, \frac{\Delta U}{\mathbf{S_t}}\Delta x\Big)$, Δx being the spacing along the wall at the trip point.

The values of the constants used in the previous definitions are the following:

$c_{b1} = 0.1355, c_{b2} = 0.622, c_{w1} = \frac{c_{b1}}{\kappa^2} + \frac{1 + c_{b2}}{\sigma}, c_{w2} = 0.3, c_{w3} = 2, c_{v1} = 7.1, c_{v2} = 5, c_{t1} = 1, c_{t2} = 2, c_{t3} = 1.2, c_{t4} = 0.5.$

$\kappa = 0.41$ is the Von Karman constant, and $\sigma = 2/3$.

Finally the eddy-viscosity itself is obtained from $\tilde{\mathbf{v}}$ by:

$$\mu_t = \rho \tilde{\mathbf{v}} f_{v1}. \tag{A.1.6}$$

A.2 Interpolation from cell centers to vertices

For quantity Q being interpolated in a vertex p from cell centers i:

$$Q_p = \frac{\sum_{i=0}^{n} Q_i \omega_i}{\sum_{i=0}^{n} \omega_i}, \tag{A.2.1}$$

with ω_i the weighting functions defined as

$$\omega_i = 1 + \lambda_x \Delta x_i + \lambda_y \Delta y_i + \lambda_z \Delta z_i. \tag{A.2.2}$$

Δx_i, Δy_i and Δz_i are the coordinates difference between the vertex p and the cell center i.

Since the interpolation should be first order accurate, it can be written:

$$Q_i = Q_p + \Delta x_i \partial_x Q_p + /Deltay_i \partial_y Q_p + \Delta z_i \partial_z Q_p. \tag{A.2.3}$$

Since Equ. A.2.1 can be written as $\sum_{i=0}^{n} \omega_i (Q_p - Q_i) = 0$, injecting Equ. A.2.3 provides:

$$\sum_{i=0}^{n} \omega_i (\Delta x_i \partial_x Q_p + \Delta y_i \partial_y Q_p + \Delta z_i \partial_z Q_p) = 0 \tag{A.2.4}$$

This value should remain valid for any value of the derivatives; therefore, selecting three particular set of derivatives provides the following equations:

$$\begin{aligned}
\sum_{i=0}^{n} \omega_i \Delta x_i &= \sum_{i=0}^{n} \Delta x_i + \lambda_x \sum_{i=0}^{n} \Delta x_i^2 + \lambda_y \sum_{i=0}^{n} \Delta x_i \Delta y_i + \lambda_z \sum_{i=0}^{n} \Delta x_i \Delta z_i = 0 \\
\sum_{i=0}^{n} \omega_i \Delta y_i &= \sum_{i=0}^{n} \Delta y_i + \lambda_x \sum_{i=0}^{n} \Delta x_i \Delta y_i + \lambda_y \sum_{i=0}^{n} \Delta y_i^2 + \lambda_z \sum_{i=0}^{n} \Delta y_i \Delta z_i = 0 \\
\sum_{i=0}^{n} \omega_i \Delta z_i &= \sum_{i=0}^{n} \Delta z_i + \lambda_x \sum_{i=0}^{n} \Delta x_i \Delta z_i + \lambda_y \sum_{i=0}^{n} \Delta y_i \Delta z_i + \lambda_z \sum_{i=0}^{n} \Delta z_i^2 = 0
\end{aligned} \tag{A.2.5}$$

which resolution yield λ_x, λ_y and λ_z.